

# Comprehensive Study of the CuF<sub>2</sub> Conversion Reaction Mechanism in a Lithium Ion Battery

Xiao Hua,<sup>†,‡</sup> Rosa Robert,<sup>†</sup> Lin-Shu Du,<sup>‡</sup> Kamila M. Wiaderek,<sup>§</sup> Michal Leskes,<sup>†</sup> Karena W. Chapman,<sup>§</sup> Peter J. Chupas,<sup>§</sup> and Clare P. Grey<sup>\*,†,‡</sup>

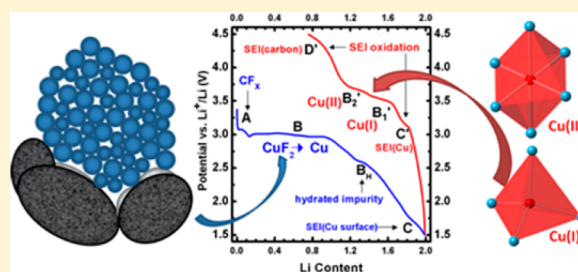
<sup>†</sup>Department of Chemistry, University of Cambridge, Lensfield Road, Cambridge CB2 1EW, United Kingdom

<sup>‡</sup>Department of Chemistry, Stony Brook University, Stony Brook, New York 11794-3400, United States

<sup>§</sup>X-ray Science Division, Advanced Photon Source, Argonne National Laboratory, Argonne, Illinois 60439, United States

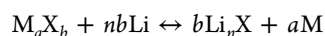
## S Supporting Information

**ABSTRACT:** Conversion materials for lithium ion batteries have recently attracted considerable attention due to their exceptional specific capacities. Some metal fluorides, such as CuF<sub>2</sub>, are promising candidates for cathode materials owing to their high operating potential, which stems from the high electronegativity of fluorine. However, the high ionicity of the metal–fluorine bond leads to a large band gap that renders these materials poor electronic conductors. Nanosizing the active material and embedding it within a conductive matrix such as carbon can greatly improve its electrochemical performance. In contrast to other fluorides, such as FeF<sub>2</sub> and NiF<sub>2</sub>, good capacity retention has not, however, been achieved for CuF<sub>2</sub>. The reaction mechanisms that occur in the first and subsequent cycles and the reasons for the poor charge performance of CuF<sub>2</sub> are studied in this paper via a variety of characterization methods. In situ pair distribution function analysis clearly shows CuF<sub>2</sub> conversion in the first discharge. However, few structural changes are seen in the following charge and subsequent cycles. Cyclic voltammetry results, in combination with in situ X-ray absorption near edge structure and ex situ nuclear magnetic resonance spectroscopy, indicate that Cu dissolution is associated with the consumption of the LiF phase, which occurs during the first charge via the formation of a Cu<sup>1+</sup> intermediate. The dissolution process consequently prevents Cu and LiF from transforming back to CuF<sub>2</sub>. Such side reactions result in negligible capacity in subsequent cycles and make this material challenging to use in a rechargeable battery.



## 1. INTRODUCTION

Lithium ion battery research on electrode materials has mainly focused on insertion compounds. The capability of these materials to host Li in their framework structure gives rise to an excellent cyclability and thus good capacity retention. However, insertion reactions typically allow only 0.5–1 electron transfer per redox-active ion, which limits their capacity. This limitation has fueled the exploration of new functional materials. Recently, much effort has been focused on binary metal oxides and fluorides (M<sub>a</sub>X<sub>b</sub>, X = O, F), which operate via a conversion mechanism forming metal (M) and Li<sub>2</sub>O or LiF phases during discharge and returning to the original M<sub>a</sub>X<sub>b</sub> phase upon charging:<sup>1</sup>



Depending on the oxidation state of the metal ion, Li incorporation involves more than one electron transfer, which leads to much higher capacities than observed for conventional insertion compounds such as LiCoO<sub>2</sub> and LiFePO<sub>4</sub>.<sup>1</sup> In the search for cathode materials, 3d transition-metal fluorides (MF<sub>x</sub>) have received the most interest due to their ability to deliver high electrochemical energy density arising from the high free energy of formation of fluorides.<sup>2</sup> Among these 3d

transition-metal fluorides, CuF<sub>2</sub> stands out as a promising candidate because it has a high specific capacity of 528 mAh/g and the highest theoretical potential of 3.55 V among all the divalent 3d transition-metal fluorides, leading to an exceptionally high specific energy of 1874 Wh/kg (cf. 600 Wh/kg for LiCoO<sub>2</sub>).<sup>2,3</sup> However, the electrochemical performance of CuF<sub>2</sub> is drastically different in practice. Its sensitivity to moisture engenders a significant challenge for material preparation and electrode fabrication. Hydrated impurities often accompany anhydrous CuF<sub>2</sub> and are responsible for significantly reducing the theoretical energy density, since their operating potentials are around 2 V instead of 3 V.<sup>4</sup> The intrinsic large band gap, arising from the high electronegativity of fluorine, makes CuF<sub>2</sub> a poor electronic conductor. To enhance the conductivity, a mixed conductive matrix (MCM) approach has been developed, in which carbon or other compounds with excellent electronic and ionic conductivity, such as MoO<sub>3</sub>, are employed to improve electronic wiring.<sup>4</sup> A full utilization of the theoretical capacity of CuF<sub>2</sub>, as well as an

Received: April 21, 2014

Revised: June 9, 2014

Published: June 11, 2014

increase of operating potential to 3 V, has been demonstrated with this approach. The improvement of the electrochemical performance is believed to be derived from a combination of nanosizing the particles and connecting each domain with a conductive matrix, which enlarges the interfacial area for Li incorporation and shortens the tunneling length for electron transport.<sup>5</sup> However, in comparison to the progress that has been made on discharge, good capacity retention after the first discharge has not yet been achieved. The mechanism underlying the electrochemical performance of conversion materials has been investigated for a variety of oxides and fluorides and has highlighted the significance of electronic and ionic transport, volume expansion, and solid–electrolyte interface (SEI) formation, in modulating the discharge/charge cycling performance.<sup>5–9</sup> However, the insight from these studies cannot be straightforwardly applied to  $\text{CuF}_2$ , owing to its distinct electrochemistry, and the sources of its irreversibility and the increasing overpotential after insertion of approximately one  $\text{Li}^+$  per formula unit upon discharge<sup>4,5</sup> still remain unclear.

In this paper, we investigate the  $\text{CuF}_2$  lithiation mechanism over a full cycle, aiming to gain a fundamental understanding of the whole electrochemical reaction. In particular, we elucidate the main factors that reduce the reversibility of this system. Due to its nanostructured nature and the extensive chemical heterogeneity of the reaction, the pathway to acquire such knowledge is challenging. A variety of phase and structural characterization techniques to extract both short- and long-range order are therefore required. Electrochemical tests including galvanostatic and cyclic voltammetry (CV) experiments are first employed to obtain a comprehensive picture of the redox reactions in different potential windows. Structural and phase information concerning copper-containing components are then obtained via in situ X-ray absorption near edge structure (XANES) and in situ pair distribution function (PDF) analyses. Ex situ solid-state nuclear magnetic resonance (NMR) is performed to investigate Li components present upon cycling. We demonstrate that NMR is a powerful approach to study phases containing either low X-ray scatterers, such as  $\text{LiF}$ , or low-concentration SEI products.

## 2. EXPERIMENTAL SECTION

**2.1. Materials Preparation.** Carbon-coated nano- $\text{CuF}_2$  ( $\text{CCN-CuF}_2$ ) was prepared by ball-milling commercial  $\text{CuF}_2$  (Sigma-Aldrich 98%) and carbon black (Ketjen Black International Co.). Two ball-milling methods were employed, planetary ball-milling (PBM) (Retsch PM 100) and high-energy ball-milling (HBM) (SPEX 8000M). Either 0.5 or 1 g of a mixture composed of  $\text{CuF}_2$  and carbon black (80:20 wt %) was prepared and placed into a milling jar in an Ar-filled glovebox. The jar was sealed with Parafilm before being transferred to the ball mill. For the PBM, a stainless steel jar (Rotec) with zirconia beads of various volume percentages (40 and 70 vol %) was used. The milling process was programmed for various time periods at different speeds (300, 500, and 600 rpm). For the HBM, a zirconia container with two zirconia balls was used and the milling was programmed for 45, 60, and 90 min.

**2.2. X-ray Powder Diffraction.** X-ray powder diffraction (XRPD) was performed on a laboratory Rigaku powder X-ray diffractometer with  $\text{Cr K}\alpha$  ( $\lambda = 2.29 \text{ \AA}$ ) as a radiation source at a  $0.12^\circ/\text{min}$  scan rate with  $2\theta$  range of  $10^\circ$ – $120^\circ$ . Samples were prepared in an Ar- or  $\text{N}_2$ -filled glovebox. The powder

samples were covered by Kapton films and sealed with vacuum grease (Dow) to minimize the exposure to moisture.  $\text{LaB}_6$  was used as an external standard reference to obtain the instrumental broadening and to remove the systematic error caused by zero shifts. Particle size analysis was performed using the Scherrer formula,<sup>10</sup> peak broadening being quantified via the integral breadth method,<sup>11</sup> i.e., by using the ratio of the peak area to the peak height of the different  $\text{CuF}_2$  reflections. Reflections with intensities of less than 10% of the maximum were neglected in this analysis. The instrumental broadening was evaluated from the integral breadths obtained from the profile fitting of the first six reflections of the  $\text{LaB}_6$  standard using second-order polynomials, while the strain-broadening effects were neglected.<sup>12</sup> Lorentzian line-shapes were used in the profile fitting for all the reflections.

**2.3. Electrochemical Characterization.** The electrochemical properties of  $\text{CCN-CuF}_2$  were evaluated with 2032 type coin cells and Swagelok cells. The cathode materials were prepared by mixing 85 wt %  $\text{CCN-CuF}_2$  (HBM of 0.5 g for 60 min) and 15 wt % carbon black (Super P). The cathode films were prepared by mixing 80 wt %  $\text{CCN-CuF}_2$ , 15 wt % Super P, and 5 wt % polyvinylidene fluoride (PVDF) as a binder in *N*-methylpyrrolidinone (NMP). The slurry was dispersed on either an aluminum or copper foil (Goodfellow) in air followed by drying in an oven at  $80^\circ\text{C}$ . Two additional batteries, with one using only Cu foil as a cathode and the other a carbon mixture (50 wt % Super P and 50 wt % Ketjen Black) directly deposited on the stainless steel current collector, were also tested for comparison purposes. Both coin cells and Swagelok cells were assembled in an Ar-filled glovebox with Li metal foil as the anode. The electrolyte consisted of 1 M  $\text{LiPF}_6$  dissolved in a mixture solution of ethylene carbonate (EC) and dimethyl carbonate (DMC) with a volume ratio of 1:1, except for one CV experiment in which ethyl methyl carbonate (EMC) was used as a solvent. Either Celgard or glass fiber (Whatman) was used as a separator. The galvanostatic cycling measurements were performed either in various potential windows or a specific capacity window at room temperature using Arbin battery cycling systems. The Li content in each sample was calculated from the theoretical discharge capacity of  $\text{CuF}_2$  ( $\text{Li} = 2.0$  for 528 mAh/g), assuming 100% Coulombic efficiency. Different cycling rates of  $C/n$  ( $n = 35, 50$  and  $100$ ) were also investigated, where  $C$  stands for theoretical specific (dis)charge capacity (mAh/g) and  $n$  represents number of hours to reach the theoretical capacity. For all the ex situ studies, the samples were obtained from powder-based coin cells. When the cells reached the desired Li content or potential, the cells were stopped and disassembled in the glovebox. The cathode powder materials were collected in a vial and rinsed with DMC to remove residual  $\text{LiPF}_6$  from the electrolyte. After drying overnight in a glovebox, the washed cathode samples were stored in a glass container under inert Ar atmosphere until required for further measurements. Galvanostatic intermittent titration (GITT) experiments were performed on a Swagelok cell under a  $C/20$  rate with a 3-h current step and a 48-h relaxation period. CV measurements were performed on coin cells in potential windows of 4.5–2.0, 4.5–1.3, 4.5–0.4, and 4.5–0 V vs lithium metal with a scan rate of 0.1 mV/s.

**2.4. X-ray Absorption Spectroscopy.** The XANES spectra were collected at beamline X19A at the National Synchrotron Light Source (NSLS) at Brookhaven National Laboratory. The measurements were performed in transmission mode using a  $\text{Si}(111)$  double-crystal monochromator, which

was detuned by 30% to minimize the presence of higher harmonics in the beam. Energy calibration was carried out by using the first inflection point in the spectra of Cu metal foil as reference (Cu K-edge, 8979 eV). A series of reference materials containing Cu atoms with different oxidation states was measured, namely CuCl, CuCl<sub>2</sub>, Cu<sub>2</sub>S, Cu<sub>2</sub>O, CuO, and CuF<sub>2</sub>.

The in situ cells were prepared using Al plates with Mylar windows.<sup>13</sup> Each cell was composed of a self-standing CCN-CuF<sub>2</sub> film [mass ratio of CCN-CuF<sub>2</sub>:Super P:polytetrafluoroethylene (PTFE) = 8:1:1] attached to an Al foil as current collector, a Li metal negative electrode with Cu mesh as current collector, a Celgard separator, and 1 M LiPF<sub>6</sub> in EC/DMC (volume ratio 1:1) as electrolyte. The in situ cell was fully discharged and then charged to a capacity corresponding to a Li content of approximately 1.5 per CuF<sub>2</sub> formula unit using a C/40 rate. A second, essentially identical, battery was then used to collect the data for the rest of the charge; a faster rate of C/17.5 and a cutoff potential of 4.1 V was used due to the limited beam time availability. The ex situ samples were prepared using coin cells cycled at C/100. Powder extracted from the dry electrode was then rubbed onto Kapton tape. The data was analyzed using IFEFFIT and the Demeter package.<sup>14</sup>

**2.5. Extracting the Pair Distribution Function from X-ray Total Scattering.** X-ray PDF analyses were performed in situ and ex situ at beamline 11-ID-B at the Advanced Photon Source (APS) at Argonne National Laboratory. The total scattering data were collected at room temperature using an amorphous Si-based 2D detector with an X-ray energy of 58 keV ( $\lambda = 0.2127 \text{ \AA}$ ). For the in situ experiment, electrode pellets of CCN-CuF<sub>2</sub> that contained 20 wt % of carbon and 20 wt % of PTFE were prepared and assembled into the AMPIX cell,<sup>15</sup> with a glass fiber as separator, a Li metal foil as counter electrode, and 1 M LiPF<sub>6</sub> in EC/DMC (volume ratio 3:7) solution (Tomiya Pure Chemical Industries) as electrolyte.<sup>16</sup> The cell was cycled under a rate of C/20 at room temperature. The ex situ experiments were performed on fine powder samples, which were sealed in Kapton capillaries filled under Ar atmosphere. The total scattering experiments were conducted in transmission geometry. A CeO<sub>2</sub> standard was used to calibrate the sample-to-detector distance and the tilt of the detector relative to the beam path. Scattering measurements for the empty Kapton capillary, as well as a reference AMPIX cell containing all the components in the same mass ratio except the active material, were also performed under the same experimental conditions to obtain the instrumental background.<sup>17</sup> Intensity data versus  $2\theta$  and  $Q$  were obtained by converting the integrated data using the Fit2D software.<sup>18</sup> The PDF data were generated using the PDFgetX2 program.<sup>19</sup> Data corrections, including background subtraction, sample self-absorption, multiple scattering, X-ray polarization, and Compton scattering, were included to obtain the normalized total scattering structure function  $S(Q)$ .<sup>20</sup> The pair distribution function  $G(r)$  was generated by direct Fourier transformation of  $Q[S(Q) - 1]$ , where the scattering wave factor is defined as  $Q = 4\pi \sin \theta/\lambda$ . A  $Q_{\text{max}}$  of  $24.0 \text{ \AA}^{-1}$  was used for ex situ experiments. In situ data were limited to a lower  $Q_{\text{max}}$  of  $19.0 \text{ \AA}^{-1}$  as the maximum accessible scattering angle was limited by the scattering aperture in the AMPIX cell.<sup>21</sup> Structure refinement and the fitting of  $G(r)$  were performed using the PDFgui software.<sup>22</sup> Previously collected scattering data for the Ni standard were processed and refined to obtain the instrumental parameters.

**2.6. Solid-State Nuclear Magnetic Resonance Spectroscopy.** <sup>7</sup>Li magic angle spinning (MAS) NMR experiments were performed on cycled CCN-CuF<sub>2</sub> samples with a 1.8 mm MAS probe designed by Samoson and co-workers on a Chemagnetic CMX-200 (4.7 T) and a Varian Infinity-Plus-360 (8.47 T) spectrometer at a <sup>7</sup>Li Larmor frequency of 77.8 and 140.2 MHz, respectively. All spectra were acquired at a spinning frequency of 38 kHz with a rotor synchronized echo sequence [ $\pi/2 - \tau - \pi - \tau - \text{acq}$ , where  $\pi/2$  and  $\pi$  represent the 90° and 180° radiofrequency (rf) pulses and  $\tau$  and acq stand for echo time and acquisition time periods, respectively]. The spectra were referenced to a standard 1 M <sup>7</sup>LiCl aqueous solution at 0 ppm. A  $\pi/2$  pulse of 2.3  $\mu\text{s}$  with a relaxation delay of 1.0 s was used on the CMX-200 spectrometer and a  $\pi/2$  pulse of 2.5  $\mu\text{s}$  with a relaxation delay of 1.0 s was used on the Varian Infinity-Plus-360 spectrometer.

<sup>19</sup>F MAS NMR experiments on cycled CCN-CuF<sub>2</sub> samples were performed with a Chemagnetic 3.2 mm probe and the 1.8 mm probe (Samoson) on the Varian Infinity-Plus-360 spectrometer at a <sup>19</sup>F Larmor frequency of 338.73 MHz, with a spinning frequency of 20 and 38 kHz, respectively. An echo sequence was used with a  $\pi/2$  pulse of 2.0  $\mu\text{s}$  on both probes. A relaxation delay of 0.2 s was used on the 3.2 mm probe and 0.5 s on the 1.8 mm probe. All spectra were referenced to a standard CFCl<sub>3</sub> at 0 ppm. <sup>19</sup>F MAS NMR experiments on commercial CuF<sub>2</sub> and HBM CCN-CuF<sub>2</sub> were performed using a 1.9 mm Bruker double resonance probe on a Bruker AVANCEIII 200 MHz (4.7 T) spectrometer at a <sup>19</sup>F Larmor frequency of 188.3 MHz. A spinning frequency of 40 kHz was used with a  $\pi/2$  pulse of 2.3  $\mu\text{s}$  and a 2.0 s relaxation delay. Spectra were referenced to the external standard LiF at -204 ppm.

Saturation recovery experiments were performed on cycled CCN-CuF<sub>2</sub> samples with the 1.8 mm probe on the Varian Infinity-Plus-360 spectrometer to measure <sup>7</sup>Li and <sup>19</sup>F spin-lattice ( $T_1$ ) relaxation times. Saturation recovery times were arrayed from 10  $\mu\text{s}$  to 1 s for each measurement. Plots of integrated signal intensity versus saturation recovery time were fit to the equation  $y = \text{amp}(1 - e^{-\tau/T_1})$  using Chemagnetics Spinsight software, where  $y$  is the integrated signal intensity, amp is the amplitude constant,  $\tau$  is the saturation recovery time, and  $T_1$  is the spin-lattice relaxation time.

The <sup>31</sup>P MAS NMR experiment was performed on a fully discharged sample (Li = 2.0) with a Bruker 2.5 mm double resonance probe on Bruker AVANCEI 400 MHz (9.4 T) spectrometer at a <sup>31</sup>P Larmor frequency of 81.0 MHz. An echo sequence with a spinning frequency of 30 kHz was used with a  $\pi/2$  pulse of 2.5  $\mu\text{s}$  and a relaxation delay of 5 s. The chemical shift was referenced to NH<sub>4</sub>H<sub>2</sub>PO<sub>4</sub> at 0.81 ppm as a secondary reference.

<sup>19</sup>F→<sup>13</sup>C cross-polarization (CP)-MAS NMR experiments were performed on the pristine CCN-CuF<sub>2</sub> sample using a Bruker 3.2 mm triple resonance probe on a Bruker AVANCEIII 700 MHz (16.5T) spectrometer. The <sup>19</sup>F→<sup>13</sup>C CP conditions were optimized on PTFE and then applied to the CCN-CuF<sub>2</sub> sample spinning at 20 kHz with a relaxation delay of 2 s and a CP contact time of 500  $\mu\text{s}$ . <sup>19</sup>F continuous wave decoupling was applied during the <sup>13</sup>C signal acquisition at an rf nutation frequency of 70 kHz.

All spectra shown in the plots are normalized with respect to the sample weight, number of scans and receiver gain.

### 3. RESULTS AND DISCUSSION

**3.1. X-ray Powder Diffraction.** Laboratory X-ray diffraction was performed on CCN-CuF<sub>2</sub> to investigate the size reduction effect induced by the different milling methods (PBM and HBM) and milling parameters (Table 1 and Figure

**Table 1. Material Preparation and Electrode Fabrication Methods**

material preparation		electrode fabrication	
		film	powder
PBM	3 h, 500 rpm with 70 vol % ZrO <sub>2</sub> beads	✓	✓
	36 h, 300 rpm with 40 vol % ZrO <sub>2</sub> beads	✓	✓
	24 h, 600 rpm with 40 vol % ZrO <sub>2</sub> beads	✓	✓
HBM	1 h, 1.0 g	×	✓
	1 h, 0.5 g	×	✓
	1.5 h, 0.5 g	×	✓

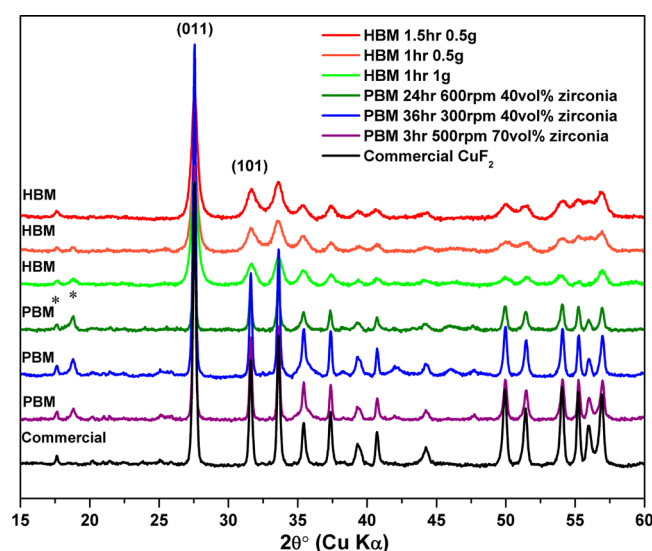


**Figure 1.** Laboratory XRD patterns for commercial CuF<sub>2</sub> and CCN-CuF<sub>2</sub> nanocomposites prepared under various conditions. The two main CuF<sub>2</sub> reflections, (011) and (101), are labeled. The two reflections marked with asterisks at low angles correspond to impurity phases. The reflection at 18.8° 2θ is assigned to Cu(OH)F and/or CuF<sub>2</sub>·2H<sub>2</sub>O. HBM, high-energy ball mill; PBM, planetary ball mill.

1). An XRPD pattern for the commercial monoclinic CuF<sub>2</sub> phase ( $P2_1/n$ ) is given for comparison, and an analysis of the patterns shows that this phase is dominant in all the samples. The HBM method leads to significant peak broadening in all the CuF<sub>2</sub> patterns. However, no discernible difference with respect to the peak width was found for the different milling times. In comparison, the reflections in the patterns for the PBM samples showed either less (24 h 600 rpm, 40 vol % ZrO<sub>2</sub> beads) or very little broadening (36 h, 300 rpm, 40 vol % ZrO<sub>2</sub> beads and 3 h, 500 rpm, 70 vol % ZrO<sub>2</sub> beads) compared to commercial CuF<sub>2</sub>, even though a high milling rate and a long duration of milling time was used. Assuming that strain broadening gives a negligible contribution to the peak width, these observations suggested that HBM is a more effective approach compared to PBM to reduce the particle size of CuF<sub>2</sub>. The Scherrer formula<sup>10</sup> was employed to calculate the average

particle size for the “HBM 1 h 0.5 g” sample, giving an average particle size of about 10 nm. However, the observation of an extra Bragg reflection at 17.6° 2θ and some very weak features between 17° and 27° 2θ in all the samples suggest the presence of impurities. The broad peak at about 18.8° 2θ seen after ball-milling is assigned to either the hydrated phase Cu(OH)F (main reflection at 18.9° 2θ) and/or CuF<sub>2</sub>·2H<sub>2</sub>O (main reflection at 18.4° 2θ). The intensity of this reflection was less pronounced in the HBM samples, probably because the much shorter milling time leads to less moisture contamination.

**3.2. Electrochemical Characterization.** The electrochemical performances of both film- and powder-based cathodes containing the CCN-CuF<sub>2</sub> obtained with various milling parameters were investigated by galvanostatic cycling to select the optimal material preparation and electrode fabrication method (see Table 1). All the film-based batteries show a plateau at a potential of around 2 V in the first discharge profile (Figure 2), lower than that for the powder-based

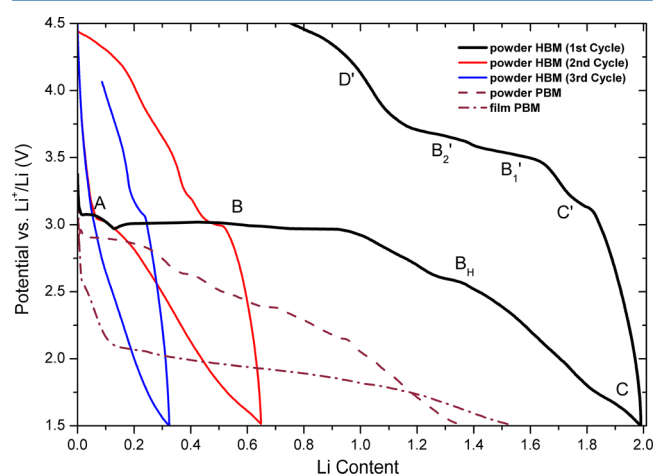


**Figure 2.** Representative potential profiles for CCN-CuF<sub>2</sub> electrodes produced using different material preparation and electrode fabrication methods. Solid (bold black, first cycle; red, second cycle; blue, third cycle), dash, and dash-dot profiles correspond to the potential profiles for the HBM powder-based battery, the PBM powder-based battery, and the PBM film-based battery, respectively. All batteries were cycled with a rate of C/100. The same labels A–D are used to mark the same processes in all subsequent electrochemistry figures. The assignments of the labels are listed in Table 2.

batteries. This is ascribed to the formation of a hydrated CuF<sub>2</sub> phase during film fabrication.<sup>4</sup> Thus, the powder-based electrodes were employed for further investigation. Comparing the CCN-CuF<sub>2</sub> powder-electrodes obtained via PBM and HBM methods, the PBM CCN-CuF<sub>2</sub> powder-electrode exhibits a shorter plateau with a lower potential at around 2.8–2.9 V. After reaction with ~0.3 mol of Li, the operating potential gradually slopes down, suggestive of an increase in overpotential. In contrast, following a preplateau feature A, the potential plateau for the HBM CCN-CuF<sub>2</sub> powder-electrode remains at 3.0 V (B) for up to one Li insertion. (The same labels A–E, B<sub>1</sub>–E') are summarized in Table 2). A sloping voltage is seen after 1 mol of Li incorporation. The significant difference in the electrochemical performance between the PBM and HBM powder samples can be ascribed to the smaller particle size and the fewer hydrated impurities

Table 2. Assignments of the Labels in the Electrochemistry Plots<sup>a</sup>

first discharge			first charge		
A	3.3 V <sup>b</sup>	CF <sub>x</sub> lithiation	B <sub>1</sub> '	3.58 V <sup>b</sup>	Cu(0) to Cu(I) oxidation
B	3.25 V <sup>d</sup>	CuF <sub>2</sub> one-step lithiation forming Cu + 2LiF	B <sub>2</sub> '	3.8 V <sup>b</sup>	Cu(I) to Cu(II) or Cu(0) to Cu(II) oxidation
B <sub>H</sub>	2.5 V <sup>c</sup>	reaction of the hydrated CuF <sub>2</sub> phase	C'	3.2 V <sup>b</sup>	oxidation of SEI formed in process C
C	1.7 V <sup>b</sup>	electrolyte (mainly DMC) decomposition on Cu surface	D'	4.4 V <sup>b</sup>	oxidation of SEI formed in process D
D	0.65 V <sup>b</sup>	electrolyte (EC/DMC) decomposition on carbon surface	E'	~1.0 V <sup>b</sup>	reaction related to carbon, correlated with process E
E	0.4–0 V <sup>b</sup>	reactions related to carbon			

<sup>a</sup>The potentials of these processes extracted from the galvanostatic and CV experiments are given. The equilibrium potential from GITT is given for the main conversion reaction. <sup>b</sup>CV. <sup>c</sup>Galvanostatic. <sup>d</sup>GITT.

present in HBM CCN-CuF<sub>2</sub>, which both appear to lead to a smaller polarization overpotential. There are two distinct processes at around 2.5 V (B<sub>H</sub>) and 1.8 V (C) in the sloping region of the HBM electrode potential profile. Full capacity is reached at about 1.5 V. These potential profiles are similar to those reported in the literature previously,<sup>4,5</sup> and thus, the following studies are performed on the samples prepared by the HBM method. Because no discernible difference in electrochemistry was seen for the different HBM methods, a 0.5 g weight loading of composite and a 1 h ball-milling duration were used in all subsequent studies.

The first charge curve for the sample HBM CCN-CuF<sub>2</sub> shows a specific charge capacity of 316 mAh/g, which is equivalent to 1.2 mol Li content per formula unit. The charge process starts with a steep rise in potential until it reaches a preplateau slightly above 3 V (C'). This is followed by a flatter region between 3.5 and 3.8 V (B<sub>1</sub>' and B<sub>2</sub>'), and then the potential rises again until the upper limit used here of 4.5 V (D), leading to a large potential hysteresis in the first cycle. The specific capacities of the subsequent discharge/charge cycles are reduced significantly, and no plateaus are present in any of the subsequent discharge steps. Only about 32% and 16% of the specific capacity were obtained in the second and third discharge process, respectively. After the third cycle, the specific capacity of the HBM CCN-CuF<sub>2</sub> cathode is negligible.

The GITT curve for the first cycle is shown in Figure S1 (Supporting Information, SI). The equilibrium potential after relaxation at the beginning of discharge and at the end of charge is almost identical. During the first discharge, before 1.2 mol of Li reaction, a constant equilibrium potential is observed at ca. 3.25 V, indicative of a two-phase reaction. When the intermittent discharge is continued beyond approximately 1.2 Li, a drop of the equilibrium potential is observed, suggesting that additional processes are occurring. Upon charge, the equilibrium potential gradually increases to 3.25 V with decreasing Li content until the operating potential reaches the upper limit of 4.5 V.

In order to study the electrochemical processes taking place upon cycling in further detail, CV measurements were performed for different potential windows of 4.5–2.0, 4.5–1.3, and 4.5–0.4 V vs lithium metal (Figure 3). Figure 4 shows the electrochemical profile for the CCN-CuF<sub>2</sub> cathode discharged to 0 V along with the potential curves for a Cu foil and carbon mixture cathode. In Figure 3, all three curves exhibit a small reduction peak at around 3.3 V (A) and a large reduction peak at 2.6 V (B) in the cathodic sweep. The 3.3 V peak is tentatively ascribed to reaction with the possible impurities in HBM CCN-CuF<sub>2</sub>, and it will be discussed in more detail in section 3.5. The peak at 2.7 V corresponds to the lithiation of CuF<sub>2</sub> to form Cu metal. Comparing the redox pairs found in the potential window of 4.5–1.3 V to those in the

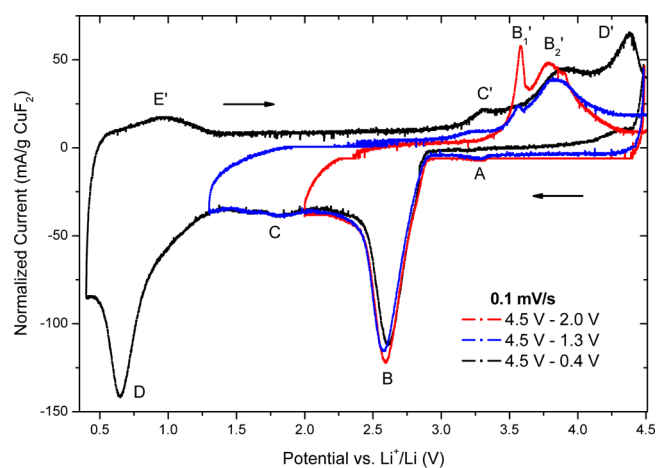


Figure 3. First sweeps in the cyclic voltammograms of a CCN-CuF<sub>2</sub> electrode for different potential windows (red, 4.5–2.0 V; blue, 4.5–1.3 V; black, 4.5–0.4 V) with a scan rate of 0.1 mV/s. The current is normalized per gram of active material.

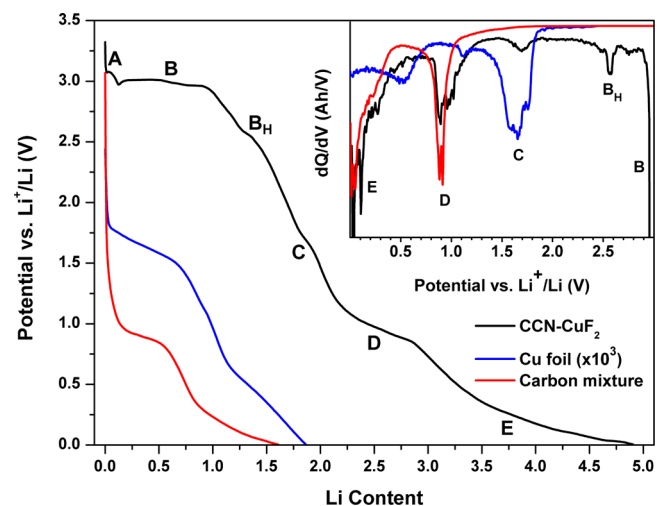


Figure 4. Potential profiles for batteries using CCN-CuF<sub>2</sub> (black), Cu foil (blue), and carbon mixture (red) as cathode materials discharged to 0 V. The capacity from Cu foil has been scaled by 10<sup>3</sup> for a better comparison. The inset shows a dQ/dV plot converted from the potential profiles.

potential window of 4.5–2.0 V, we make the following observations: (i) the small feature at around 1.7 V (C) is correlated to the extra oxidation peak at 3.2 V (C') and (ii) the anodic current for the oxidation peak at 3.58 V (B<sub>1</sub>') decreases following discharge to 1.3 V. With the cutoff potential lowered to 0.4 V, another intense reduction peak appears at about 0.65 V (D), corresponding to plateau D in Figure 4. On the anodic

sweep, new features are observed: (i) a broad feature at around 1.0 V ( $E'$ ), (ii) the absence or significant reduction of the oxidation peak at 3.58 V ( $B_1'$ ), and (iii) an intense oxidation peak at 4.4 V ( $D'$ ). The reduction processes at 1.7 V (C) and 0.65 V (D) are tentatively ascribed to the cathodic formation of SEI due to the reduction of electrolyte, while the oxidation peaks at 3.2 V ( $C'$ ) and 4.4 V ( $D'$ ) can be attributed to the oxidation of the SEI products formed during the C and D processes.<sup>23–27</sup> A recent CV study of the fluoride conversion material  $\text{BiF}_3$  ascribed the reduction peaks at 1.7 and 0.8 V to EC and DMC decomposition, respectively.<sup>28</sup> However, the reduction feature C is also present in our CV experiment on the 1 M  $\text{LiPF}_6/\text{EMC}$  electrolyte (an EC free) system, which indicates that the reduction process C in our system is likely dominated by the linear carbonate DMC rather than cyclic carbonate EC. The  $dQ/dV$  plot obtained from the reference cathodes, copper foil and carbon (inset of Figure 4), reveals that peak C is only observed when Cu is present while peak D occurs when carbon is used, suggesting that the decomposition of the electrolyte on the surface of the cathode occurs at different potential values for different components of the cathode. We can thus attribute reaction C to the electrolyte decomposition, possibly dominated by DMC decomposition, on the copper surface, and D to EC/DMC decomposition on the carbon surface. The features E in the cathodic sweep and  $E'$  in the forward anodic sweep, which are only present in the CV with a large potential window (4.5–0.4 or 4.5–0.0 V), are also attributed to the electrolyte reactions related to carbon.<sup>29–32</sup>

In the CVs obtained with a potential window of 4.5–2.0 and 4.5–0.0 V vs lithium metal (Figure S2, SI), a large reduction of current response is observed after each sweep, reflecting the capacity loss and poor cyclability of  $\text{CCN-CuF}_2$  in both potential windows. In addition to the intensity reduction or the loss of peak B (the conversion reaction of  $\text{CuF}_2$ ), both peaks C and D show less pronounced intensities in the subsequent sweeps. This is ascribed to the passivation effect of the SEI layer, which provides kinetic stability to the electrolyte against further reduction upon successive scans, resulting in a smaller current.<sup>33</sup>

**3.3. XANES.** Many detailed XANES analyses are performed based on the studies of well-characterized model compounds as references, and the characteristic near-edge structure for Cu(I) and Cu(II) are often utilized for fingerprinting the valence state and their coordination environments.<sup>34</sup> To this end, a series of Cu-containing reference compounds were first measured and their normalized XANES spectra along with their corresponding first derivatives are shown in parts a and b of Figure 5, respectively, the first peak in the derivative indicating the K-edge position of each Cu species. The edge positions are located at 8979 and 8980–8982 eV for Cu and Cu(I) species, respectively, while Cu(II) compounds all have even higher K-edge energies. Among the Cu(II) compounds,  $\text{CuF}_2$  shows the highest edge energy of about 8988.8 eV, due to the larger electronegativity of F (and thus lower electron density nearby  $\text{Cu}^{2+}$ ) as compared to O and Cl.

Figure 6 shows the first derivative of the Cu K-edge XANES spectra for HBM  $\text{CCN-CuF}_2$  and commercial  $\text{CuF}_2$ . A small peak corresponding to the pre-edge feature in the  $\text{CuF}_2$  XANES spectrum is observed at 8976 eV, which is assigned to the  $1s-3d$  electric-dipole-forbidden quadrupole-allowed transition.<sup>34,35</sup> The other two peaks at about 8989 and 8993 eV were attributed to the  $1s-4p_z$  and  $1s-4p_{x,y}$  dipole-allowed transitions, respectively, in an earlier polarization-dependent

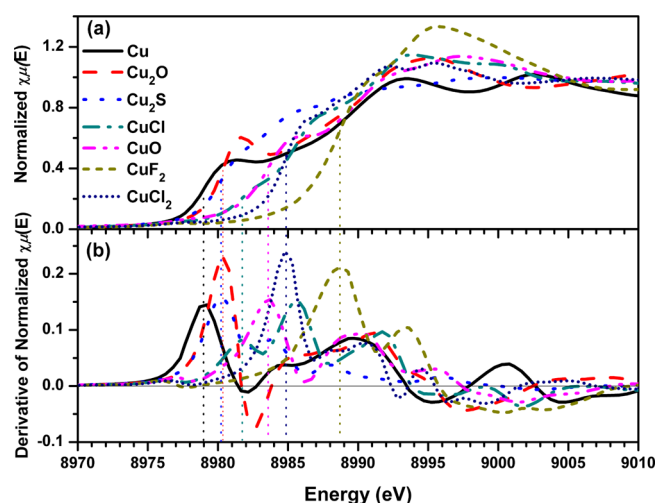


**Figure 5.** (a) Normalized Cu K-edge XANES spectra of Cu metal and Cu reference compounds ( $\text{Cu}_2\text{O}$ ,  $\text{Cu}_2\text{S}$ ,  $\text{CuCl}$ ,  $\text{CuO}$ ,  $\text{CuF}_2$ ,  $\text{CuCl}_2$ ). (b) First derivatives of the normalized Cu K-edge XANES spectra shown in part a. The positions of the edge energies of each reference material are marked with dotted lines.

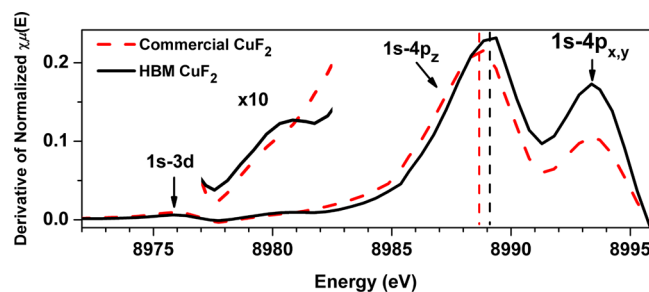


**Figure 6.** First derivatives of the normalized Cu K-edge XANES spectra of commercial  $\text{CuF}_2$  (red dash) and HBM  $\text{CCN-CuF}_2$  (black solid). The inset shows a magnification ( $\times 10$ ) of the spectra in the same energy region. An additional absorption peak is present at around 8980 eV in HBM  $\text{CCN-CuF}_2$ , suggestive of the presence of  $\text{Cu}^+$  components.

XAS study.<sup>36</sup> A weak peak at about 8980 eV is observed in the first-derivative spectrum for the HBM  $\text{CCN-CuF}_2$  sample but is absent in the commercial  $\text{CuF}_2$  spectrum. On the basis of the analysis of the reference spectra, this peak can be ascribed to the presence of a Cu(I) species introduced by the ball-milling procedure. The Cu(I) impurity might arise from a reduction process caused by the presence of carbon at the elevated temperatures that are induced by the HBM process. This Cu(I) species is either present in sufficiently low quantities and/or is amorphous so that it could not be detected by XRPD. In addition, a positive shift of 0.4 eV in the edge-energy was found for HBM  $\text{CCN-CuF}_2$  relative to commercial  $\text{CuF}_2$ , possibly indicating a structural disorder after ball-milling and/or an overlap with a second impurity component.

The normalized Cu K-edge XANES spectra for in situ discharge and charge, including the Cu metal reference, are shown in parts a and b of Figure 7, respectively. The insets show the electrochemistry and the mole fraction of the  $\text{CuF}_2$  component extracted from linear combination analysis (LCA) of the XANES spectra using the Cu metal and  $\text{CuF}_2$  reference spectra. The corresponding first derivatives of the normalized difference XANES spectra are shown in Figure 7c,d. Upon discharge, the peak at around 8981 eV, which corresponds to

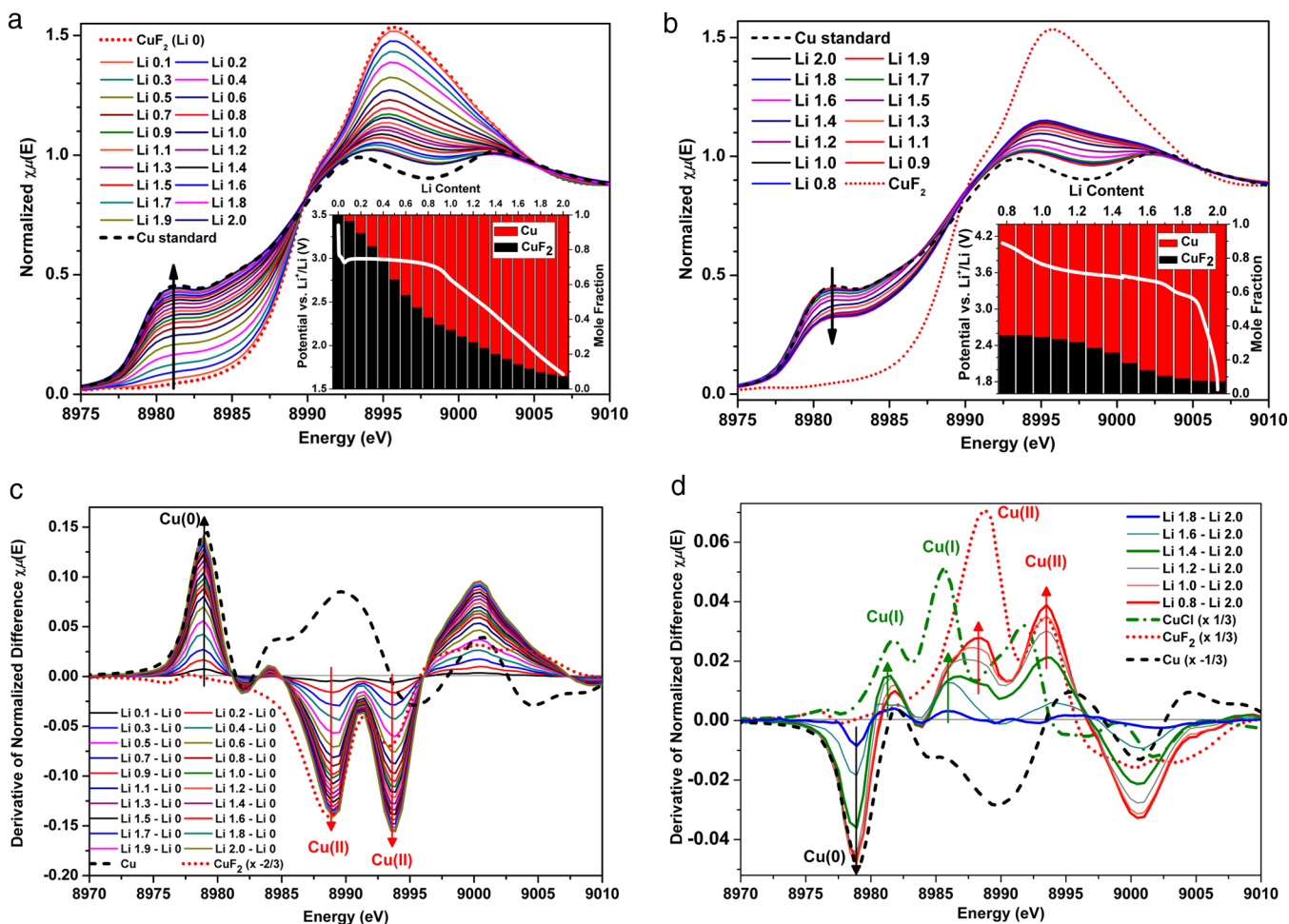


**Figure 7.** The normalized Cu K-edge XANES spectra observed in situ on (a) discharge and (b) charge. The spectrum for Cu metal reference is included. Black arrows indicate the direction of evolution of the Cu phase. The insets show the electrochemistry and the mole fractions of the  $\text{CuF}_2$  component extracted from the LCA of the corresponding XANES spectra using the spectra of Cu metal and  $\text{CuF}_2$  as references. For the LCA on charge, a three-standard fit using  $\text{Cu}^{\text{I}}\text{Cl}$  as the third standard was also attempted, which is shown in Figure S3j (SI). (c) The corresponding first derivatives of the normalized difference XANES spectra shown in parts a, b. (d) Select first derivatives of the normalized difference XANES spectra shown in part b. The difference spectra are obtained by subtracting the initial XANES spectrum (Li 0 on discharge and Li 2.0 on charge) from the subsequent spectra (shown in part a) obtained on cycling, e.g., “Li 0.5 – Li 0” in part c corresponds to a subtraction of spectrum Li 0 from Li 0.5 (a); the derivative plots show the change in the various components. Three spectra, “Li 1.8 – Li 2.0”, “Li 1.4 – Li 2.0”, and “Li 0.8 – Li 2.0”, have been highlighted in part d, so as to allow a more ready comparison with the first derivatives of the normalized XANES spectra of the  $\text{CuCl}$  and  $\text{CuF}_2$  references. The magnitudes of the reference spectra have been scaled with the coefficients shown in the brackets. Arrows indicate the direction of evolution of the first-derivative peaks from various components.

the 1s–4p transition for Cu metal, was observed to grow,<sup>37</sup> consistent with the reduction of  $\text{Cu}^{\text{II}}\text{F}_2$  to Cu metal. The presence of an isosbestic point indicates a two-phase conversion reaction. Meanwhile, the two main peaks identifying  $\text{CuF}_2$  components grow in negative intensity (in the first derivative of difference XANES; Figure 7c) due to the reduction in phase fraction of  $\text{CuF}_2$ . Note that the overlap of the first derivatives of Cu metal and  $\text{CuF}_2$  in this energy range results in different line shape for the two first-derivative peaks for  $\text{CuF}_2$  in the composite as compared to the  $\text{CuF}_2$  reference. Such alteration of the peak line shape from the superimposition of multiple spectra is also present in the first derivative difference spectra upon charge. No peaks between 8980 and 8982 eV corresponding to Cu(I) species were observed. These observations confirm that the discharge process involves a single-step conversion reaction that proceeds directly from  $\text{CuF}_2$  to Cu without forming any intermediate Cu(I) species. On the basis of the mole fraction from the LCA (inset of Figure

7a), the conversion reaction starts to slow down at Li = 0.9, which coincides with the kink in the potential profile, indicating that side reactions are occurring in the sloping region. This is consistent with the GITT results, confirming that multiple reactions are taking place at this point. Consequently, about 8% of  $\text{CuF}_2$  remains unreacted when the theoretical discharge capacity is reached.

The XANES spectra of HBM CCN- $\text{CuF}_2$  cathode upon charge shows a reduction in intensity of the Cu peak at about 8981 eV (Figure 7b) and an increase in negative intensity of the peak in the first derivative at 8979 eV (Figure 7d), indicating the loss of Cu metal. The positive peaks in the first-derivative difference spectra are attributed to the formation of higher oxidation state Cu species. Among those peaks, the ones at 8982 and 8986 eV reach a maximum at Li = ~1.2–1.4. The peak at 8982 eV then starts to decrease while the peak at 8986 eV stops growing in intensity. However, the peaks at 8986 and 8993 eV maintain a steady growth until a capacity of Li = 0.8 is

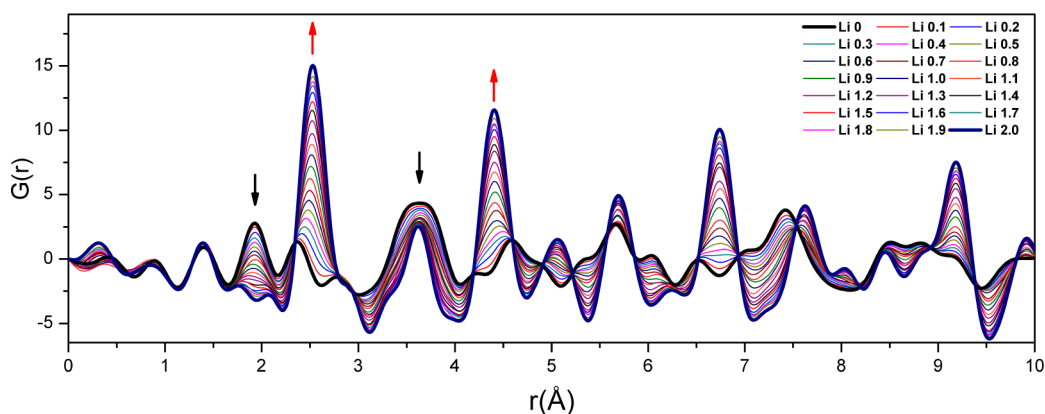


**Figure 8.** In situ PDFs for CCN-CuF<sub>2</sub> on the first discharge with initial and end states highlighted in bold. Black and red arrows indicate a decrease and increase in intensity, respectively.

reached. All three Cu(I) reference compounds studied here (Figure 5) give rise to edge energies between 8980 and 8982 eV, and the line shape of the Li 1.4 – Li 2.0 first derivative shows the closest resemblance to that of the CuCl reference. According to the fingerprinting theory for Cu(I) species proposed by Kau et al.,<sup>34</sup> the peaks seen at 8982, 8986, and possibly 8993 eV for the Li 1.4 – Li 2.0 spectrum can be assigned to a Cu(I) species with tetrahedral geometry, similar to that found in CuCl. Some possible assignments can be envisaged: (i) Cu<sup>I</sup>F instinctively comes to mind, since the Cu<sup>+</sup> cation is formed in a F<sup>-</sup>-rich system (However, as the only missing member in the cuprous halides family, CuF is not thermodynamically stable.),<sup>38–40</sup> (ii) a structure containing Cu<sup>I</sup>F<sub>4</sub><sup>3-</sup> tetrahedra, and (iii) an oxygen-containing Cu(I) species<sup>41</sup> with oxygen originating from the impurities in the composites and electrolyte. As charging proceeds, an intensity reduction of the 8982 eV peak and a growth of the 8986 and 8993 eV peaks are observed, which indicate a further oxidation of Cu or Cu(I) to a Cu(II) species where the Cu local environment is similar to that in the CuF<sub>2</sub> structure. Principal component analysis (PCA) and target transformation (TT) were performed on the XANES spectra obtained on charge and their first derivatives, to determine the number and nature of the distinct phases (Figure S3, SI).<sup>42,43</sup> The results demonstrate that while the first two components dominate the spectra in the edge region (~8980–8990 eV), at least one more component appears above the noise in the energy range corresponding to Cu(I) and Cu(II), suggesting the presence of a third phase. This phase is difficult to identify; however, the TT results reveal that it contains Cu(I) in a local environment close to that found in tetrahedrally coordinated Cu(I) in CuCl. LCA was then performed with a three-component fit using Cu<sup>I</sup>Cl as the third standard (Figure S3j, SI) and was compared to an LCA with two components employing only Cu(0) and Cu<sup>II</sup>F<sub>2</sub> as standards (Figure S3i, SI). Both results show that a large decrease in the Cu(0) fraction and an increase in the Cu(II) fraction occur from Li = ~1.8 to 1.0, corresponding to the region around 3.6 V (B<sub>1</sub>' and B<sub>2</sub>') in the galvanostatic curve; this is ascribed to the Cu(0) → Cu(II) oxidation process. The evolution of the Cu(I) fraction is captured in the three-standard fit, which shows the formation of Cu(I) species from the beginning of charge until a capacity of around Li = 1.5; this is followed by a further oxidation to Cu(II).

**3.4. X-ray PDF.** Due to the limited domain size of nanomaterials, their structures are not easily studied by a

conventional crystallographic approach using Bragg scattering. To investigate the phase transformation in an atomic scale, PDF analysis of X-ray total scattering data is employed. The experimental in situ PDFs for the first discharge, first charge, and second discharge are shown in Figures 8, S4a, and S4b (SI), respectively. The corresponding electrochemistry for the first discharge is shown in Figure 9b. Note that the electrochemistry

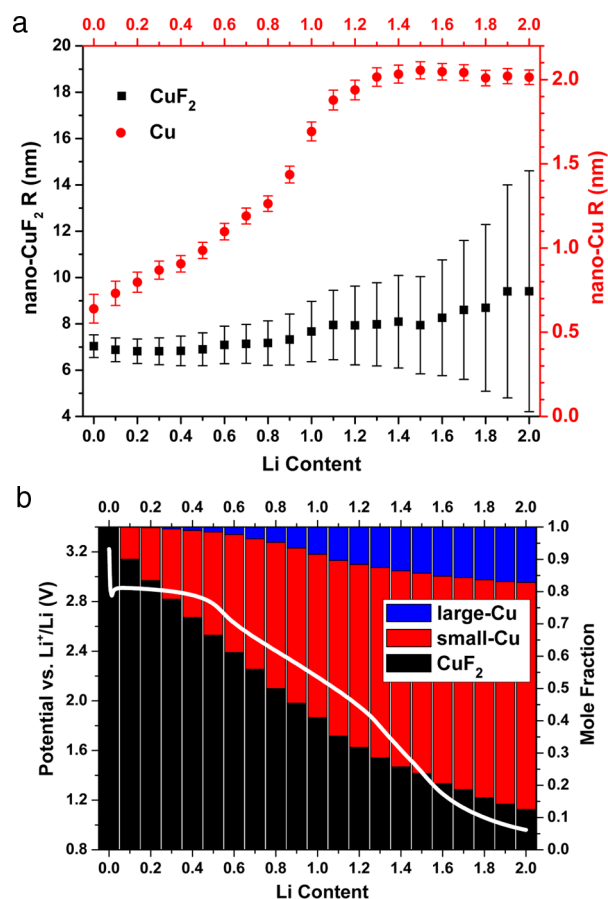


**Figure 9.** (a) The evolution of the particle sizes from the initial structure refinement (no particle size constraints applied) and (b) the phase mole fractions from the final structure refinement against the PDFs on the first discharge shown in Figure 8. The white potential profile in part b illustrates the corresponding potential curve for the in situ battery.

shows a higher overpotential than that obtained from a regular coin cell or in the in situ XANES experiment. This is attributed to the higher current rate ( $C/20$ ) used in the in situ PDF measurement, although the different cell design may also result in the increased overpotential. The data at the beginning of the discharge,  $\text{Li} = 0$ , is dominated by the PDF of the  $\text{CuF}_2$  phase (Figure 8). The two peaks at 1.9 and 2.3 Å, which correspond to the four equatorial and two elongated axial Cu–F bonds, respectively, reflect the Jahn–Teller distortion for  $\text{Cu}^{2+}$  ( $3d^9$ ). The broad features at around 3.6 Å correspond to the distances between the  $\text{Cu}^{2+}$  and the  $\text{Cu}^{2+}$  and  $\text{F}^-$  ions in the neighboring octahedra. Analysis of the in situ data indicates a particle size of about 7.0 nm for pristine CCN- $\text{CuF}_2$ , whereas the structural refinement against ex situ PDF for pristine CCN- $\text{CuF}_2$  indicates a size of 8.3 nm, both of which are quite consistent with the value obtained in the Scherrer analysis.

The PDF for the end of the discharge,  $\text{Li} = 2.0$ , has peaks at 2.6, 3.6, and 4.4 Å, which match the Cu–Cu distances in the first, second, and third coordination shell for the face-centered cubic (fcc) Cu phase, indicating the formation of Cu metal. No additional atom pairs from other phases were observed. The phase transformation from  $\text{CuF}_2$  to Cu is evident in the reduction of the peak intensity for the  $\text{CuF}_2$  phase and the growth in intensity for Cu metal.

The phase mole fractions and the evolution of the particle sizes upon discharge were evaluated from the refinement of structural models against the corresponding PDFs, where a bimodal distribution of “small” and “large” Cu particles was employed as the simplest model to describe a nonuniform particle size for the Cu phase.<sup>7</sup> Initial refinements varied the particle size to establish an appropriate constraint for particle size and more reliable phase fractions in the final structure refinement. The result of this refinement (Figure 9a) shows that the small Cu particles increase in size from 0.7 to 2 nm and then stop growing after a capacity of  $\text{Li} = 1.0$  is reached. In contrast, the size for large Cu particles is greater than 10 nm, and their size is larger than can be reliably determined from the X-ray PDF data. The  $\text{CuF}_2$  particle size remains essentially unchanged. The final structure refinement was then performed with the size of the  $\text{CuF}_2$  and small Cu particles being constrained to 7 and 2 nm, respectively, while the size of large Cu particles was not refined. The final  $\text{CuF}_2$  phase fractions of  $\text{CuF}_2$  (Figure 9b) show a trend that is consistent with in situ XANES LCA results: upon discharge, the  $\text{CuF}_2$  reacts forming mostly small Cu particles. The conversion of  $\text{CuF}_2$  starts to slow down around  $\text{Li} = 1.0$ . About 12% of the  $\text{CuF}_2$  is left when the theoretical capacity is reached. To examine the reaction at even lower potentials, ex situ PDF was performed on samples with capacities beyond those expected based on the  $\text{CuF}_2$  conversion reaction, i.e.,  $\text{Li} = 3.0$  and  $\text{Li} = 4.9$ , which correspond to discharge voltages at 0.75 and 0 V, respectively. The  $\text{CuF}_2$  mole fraction from the structure refinement against the corresponding PDFs is shown in Figure 10, which shows that the  $\text{CuF}_2$  fraction remains essentially constant in this voltage window (i.e., during process E).

The PDFs for the first charge (Figure S4a, SI) and second discharge (Figure S4b, SI) show only small changes that are dominated by the evolution of the Cu metal phase. Even though no discernible atom pairs from the  $\text{CuF}_2$  phase are readily observed, a structure refinement using Cu metal and  $\text{CuF}_2$  phases reveals an increase of 12.5% in  $\text{CuF}_2$  phase fraction for the first charge (Figure S4c, SI), and a decrease of 8% for the second discharge (Figure S4d, SI). Note that any

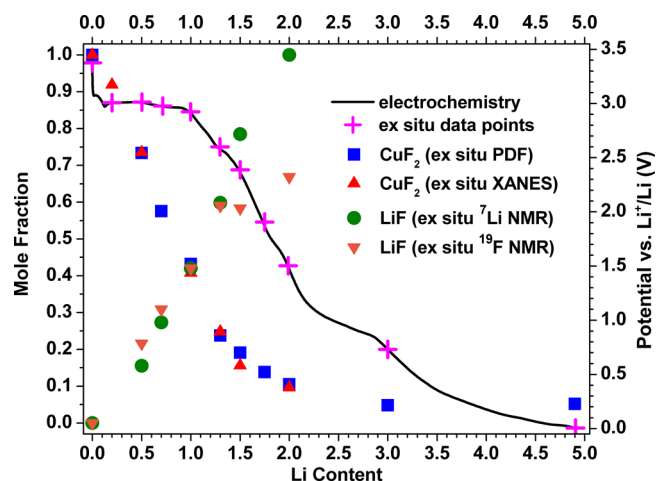


**Figure 10.** Pink crosses denote the discharged states where the samples were collected for ex situ experiments. The  $\text{CuF}_2$  mole fractions are extracted from the LCA of the ex situ XANES (red triangles) data and the structural refinements using the ex situ PDFs (blue squares). The LiF mole fractions (relative to the amount of LiF at the end of discharge) are evaluated from the integration of normalized  $^7\text{Li}$  (green circles) and  $^{19}\text{F}$  (orange inverted triangles) NMR spectra shown in Figure S6 (SI); (the  $^{19}\text{F}$  data is scaled by a factor of 0.67 in order to draw a direct comparison between the LiF mole fractions obtained from the  $^7\text{Li}$  and  $^{19}\text{F}$  NMR).

ionic Cu(I) or Cu(II) species present in the liquid electrolyte will also contribute to the PDF but will only give rise to peaks from any directly bound Cu–X ( $X = \text{F}, \text{O}$ ) species. These correlations are difficult to separate from the first Cu–F correlation in the solid  $\text{CuF}_2$  phase. Therefore, the structural model used for the PDF refinement includes only solid Cu and  $\text{CuF}_2$  phases, even though the XANES analysis suggests that a small amount of Cu(I) is present at intermediate states of charge.

To gain a better understanding of the cycling behavior of the HBM CCN- $\text{CuF}_2$  electrode, a second in situ cell was cycled at a  $C/10$  current rate. This experiment allows the structural changes of the HBM CCN- $\text{CuF}_2$  electrode during the first four discharge/charge cycles to be observed in operando (Figure 11a). The electrochemistry for this battery (Figure S5, SI) shows a very similar potential profile but with a slightly higher overpotential as compared with the cell cycled at a  $C/20$  rate in the previous experiment. The change of current rate alters the kinetics of the reaction, without appearing to change the reaction pathway significantly.

The Cu phase is the major contribution to all the patterns obtained at the end of discharge and charge. The intensities of the Cu–Cu correlations (at 2.5 and 4.3 Å) increase in the PDF patterns at the end of discharge as a function of cycle number, decreasing slightly on charge. A small broad feature at around 2 Å for the end of the first charge is observable, suggestive of an oxidized copper phase. Very small positive shifts (varying between  $\sim 0.02$  and  $0.05$  Å) in the peak positions of the PDFs due to Cu are observed between the end of charge and those at the end of discharge, which may be related to differences in the size of the Cu particles. These shifts are not caused by the growth of a Cu phase on the anode. If this phase were present, it would be located at a different (larger) sample-to-detector distance due to the geometry of the in situ experiment and AMPIX cell. This would result in small negative shifts of the

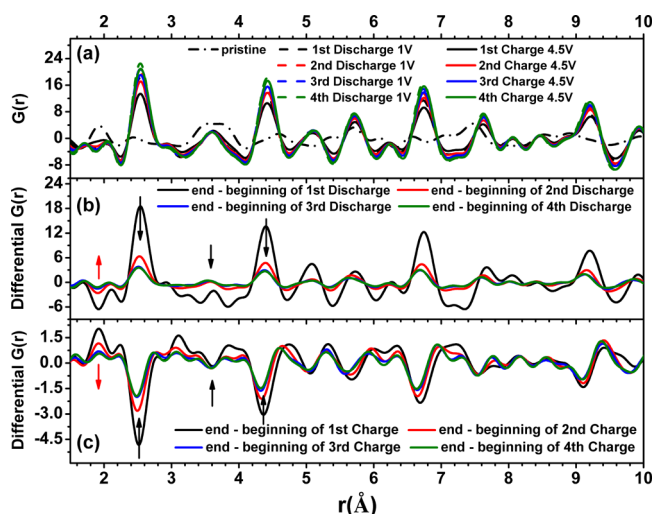


**Figure 11.** (a) Select in situ PDFs for CCN-CuF<sub>2</sub> measured for four cycles. Only the PDFs for the beginning and the end state of each cycling steps are shown. Differential PDFs on each discharge (b) and charge (c) step, obtained by subtracting the PDF of the end state from the PDF of the beginning state of each cycling step. Black and red arrows indicate the atom pairs corresponding to the Cu and CuF<sub>2</sub> phases, respectively.

Cu–Cu correlations as compared to those observed for Cu formed on the positive electrode.

The phase evolution can be seen more clearly by following the differential PDFs, obtained by subtracting the beginning from the end of each discharge or charge, where positive peaks indicate that phase(s) are being formed while the negative peaks represent the phase(s) that are reacting in each discharge (Figure 11b) and charge (Figure 11c) process. In Figure 11b, the three positive peaks corresponding to Cu–Cu correlations in the first, second, and third coordination shell of an fcc-Cu phase show the formation of Cu metal upon each discharge step. However, the magnitude of the peaks is drastically reduced in the subsequent discharge steps, indicating that less Cu forms in the corresponding process. This is consistent with the decrease in specific capacity of the corresponding discharge steps in the electrochemistry. The negative peak at 1.9 Å, from the equatorial Cu–F bond length in the distorted CuF<sub>6</sub> octahedron, reflects the reduction of the CuF<sub>2</sub> phase. This peak is evident in the first discharge, less pronounced in the second discharge, and absent in the third and fourth discharge steps, suggesting a negligible CuF<sub>2</sub> conversion in the subsequent discharge cycles. For the charge steps shown in Figure 11c, a similar phenomenon is seen where CuF<sub>2</sub> is only involved in the reaction for the first two charge steps, while Cu oxidation without forming CuF<sub>2</sub> dominates the subsequent charge processes. Comparing the magnitude of the differential PDFs within each cycle, more Cu formation during discharge is observed than Cu oxidation upon charge.

**3.5. NMR.** The composition of HBM CCN-CuF<sub>2</sub> was studied by <sup>19</sup>F MAS NMR and <sup>19</sup>F→<sup>13</sup>C CP-MAS NMR spectroscopy. Figure 12 shows the normalized <sup>19</sup>F MAS NMR spectrum of commercial CuF<sub>2</sub> and the CCN-CuF<sub>2</sub> nanocomposite. The <sup>19</sup>F signal of CuF<sub>2</sub> is not detectable because F<sup>-</sup> is directly bound to the paramagnetic Cu<sup>2+</sup> ion.<sup>5</sup> The spectrum of commercial CuF<sub>2</sub> shows only one isotropic resonance at -190 ppm, which is also present in the spectrum of the HBM nanocomposite sample. This signal was ascribed, in a previous

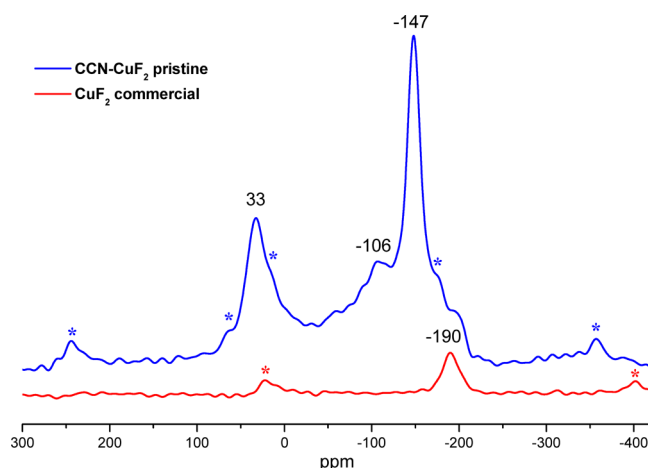


**Figure 12.** Normalized <sup>19</sup>F MAS NMR spectra of the commercial CuF<sub>2</sub> (red) and HBM CCN-CuF<sub>2</sub> (blue). Signals marked with asterisks are spinning side bands. No <sup>19</sup>F signal background from the rotor is observed.

<sup>19</sup>F NMR study, to HF adsorbed on the surface.<sup>44</sup> Three new isotropic resonances at 33, -106, and -147 ppm are present in the HBM sample, which are most likely related to the additional phases formed during the ball-milling procedure. For the preparation of the CCN-CuF<sub>2</sub> sample, commercial CuF<sub>2</sub> was mixed with carbon black and then ball-milled in a zirconia jar with zirconia beads. The collision between the milling beads and the milling jar is very likely to introduce a zirconium-containing component into the nanocomposite. Therefore, the resonance at 33 ppm in the HBM sample is tentatively assigned to β-ZrF<sub>4</sub><sup>45</sup> or a zirconium oxyfluoride,<sup>46</sup> as a result of the reaction with CuF<sub>2</sub>. A Cu(I) species was observed in the XANES spectra (Figure 6), providing evidence for Cu(II) reduction during the ball-milling process. Such reduction reaction can occur in the presence of the reducing agent carbon under elevated temperatures induced by the ball-milling: CuF<sub>2</sub> + C → CuF<sub>2-x</sub> + CF<sub>x</sub>. The resonances at -106 and -147 ppm in the HBM sample are thus assigned to -CF<sub>2</sub> and -CF fluorinated sp<sup>2</sup> C sites, respectively, on the basis of prior <sup>19</sup>F MAS NMR studies of fluorinated carbon.<sup>47–49</sup> The assignment is further confirmed by <sup>19</sup>F→<sup>13</sup>C CP-MAS NMR experiments (Figure 13) where a broad <sup>13</sup>C signal between 50

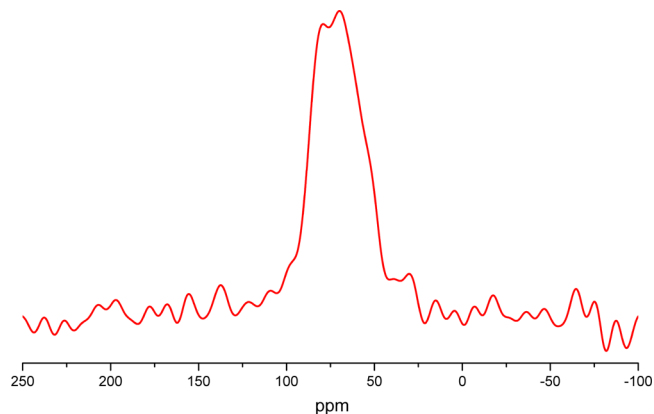


**Figure 13.** <sup>19</sup>F→<sup>13</sup>C CP-MAS NMR spectrum of HBM CCN-CuF<sub>2</sub>. No signal was present in the spectrum when the <sup>19</sup>F CP pulses were removed.

and 100 ppm is evident, similar to the  $^{13}\text{C}$  chemical shift of graphite fluorides,<sup>49</sup> demonstrating that at least some of the fluorine species are in close spatial proximity to the carbon.

A series of cycled samples was investigated by  $^7\text{Li}$  and  $^{19}\text{F}$  MAS NMR, to investigate the evolution of LiF phase, as well as to shed light on the formation of SEI products. The normalized  $^7\text{Li}$  and  $^{19}\text{F}$  NMR spectra are shown in parts a and b of Figure 14, respectively. (The  $^{19}\text{F}$  NMR for Li = 0.04 is enlarged in

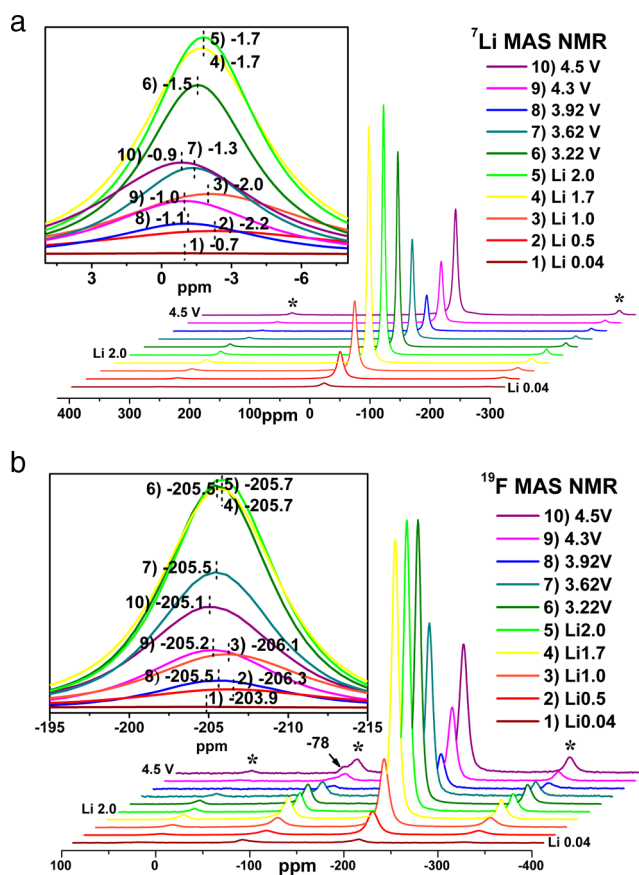


**Figure 14.** Normalized (a)  $^7\text{Li}$  and (b)  $^{19}\text{F}$  MAS NMR spectra of cycled CCN-CuF<sub>2</sub>. Signals marked with asterisks are spinning side bands. The insets show the overlay plots of the isotropic resonances of the corresponding spectra. Numbers in the insets are the values of the chemical shifts. (“Li x.x” represents the specific capacity on discharge; “x.x V” refers to the potential on charge where the samples were collected for measurement.)

Figure S6, SI.) Only one resonance is observed in the  $^7\text{Li}$  MAS NMR spectra, while more than one resonance is present in the  $^{19}\text{F}$  MAS NMR spectra. For  $^7\text{Li}$  MAS NMR, a small resonance is observed at  $-0.7$  ppm, even on the preplateau before the Cu/LiF nucleation potential dip<sup>50</sup> [region A of the voltage curve (Figure 2)] (Li = 0.04). The peak shifts to  $-2.2$  ppm at Li = 0.5 and then shifts back to  $-1.7$  ppm between Li = 0.5 and 2.0. On charge, the resonance keeps shifting toward higher ppm, reducing in intensity until the potential of the corresponding sample reaches about 3.92 V. This is followed by an increase in intensity until the end of charge. There are few Li species that give rise to negative chemical shifts other than LiF at  $-1.0$  ppm.<sup>51</sup> A resonance at  $-2.2$  ppm was similarly reported in our earlier study of CuF<sub>2</sub>, for Li = 0.5 on discharge. The resonance was assigned to LiF, the lower frequency shift being attributed to the formation of either nanosized or a thin film of LiF in

close proximity to either Cu metal or CuF<sub>2</sub>.<sup>5</sup> As the reaction proceeds, the LiF particle size becomes larger and the LiF shift is less affected by the Cu metal/CuF<sub>2</sub> (i.e., a larger portion of the LiF phase is not in close proximity to Cu/CuF<sub>2</sub>), accounting for this shift to more positive frequencies as lithiation proceeds. The increase in Li intensity at the late state of discharge is ascribed to the formation of products from LiPF<sub>6</sub> hydrolysis or electrolyte decomposition such as Li<sub>2</sub>CO<sub>3</sub> and Li<sub>2</sub>PO<sub>3</sub>F<sub>y</sub>, as suggested by our CV study, these species giving rise to more positive  $^7\text{Li}$  chemical shifts,<sup>51,52</sup> leading to a shift toward higher frequencies at the top of charge.

A similar intensity evolution is observed in the  $^{19}\text{F}$  NMR spectra, but now the spectra are not complicated by the potential overlap between LiF and any other electrolyte decomposition products. For the discharged sample Li = 0.04, three resonances are present (Figure S6, SI), which are assigned to LiPF<sub>6</sub> ( $-80$  ppm), CF<sub>x</sub> ( $-147$  ppm), and LiF ( $-204$  ppm). The LiF resonance at  $-204$  ppm dominates the spectra and the evolution of its chemical shift and intensity follow the same trend as the  $^7\text{Li}$  NMR resonance, confirming that the  $^7\text{Li}$  signal can be largely ascribed to LiF. The resonance for CF<sub>x</sub> at  $-147$  ppm becomes poorly resolved on cycling, while a new resonance at  $-78$  ppm starts to evolve at higher potential than 3.92 V upon further charge, which is assigned to Li<sub>2</sub>PO<sub>3</sub>F<sub>z</sub> according to an NMR study on the hydrolysis of LiPF<sub>6</sub>.<sup>52</sup>

Interestingly, the LiF phase formed at the early state of discharge Li = 0.04 before the Cu nucleation step is probably not associated with the formation of the metallic Cu phase but is rather associated with a reaction with the fluorinated carbon components. The Li uptake mechanism for carbon fluorides CF<sub>x</sub> depends on the nature of the C–F bond.<sup>53</sup> Our  $^{19}\text{F}$  NMR for the pristine CCN-CuF<sub>2</sub> reveals an sp<sup>2</sup> character for the carbon in the CF<sub>x</sub> phase, the carbon incorporating Li at a higher potential ( $\sim 3.2$  V) via the reaction  $\text{CF}_x + n\text{Li} \rightarrow (1-n)\text{CF}_x + n\text{C} + n\text{LiF}$ , in comparison to the CF<sub>x</sub> with a sp<sup>3</sup> carbon ( $\sim 2$  V).<sup>2</sup> The lithiation potential of the ionic CF<sub>x</sub> is consistent with the potential of the preplateau feature A in the electrochemistry curve (Figure 2).<sup>53</sup> Such fluorinated carbon phase should also be in very close proximity to the carbon matrix, since it is derived directly from the carbon. This means that the CF<sub>x</sub> should be more effectively electrically wired than CuF<sub>2</sub>. Note that the LiF formed in the reaction with CF<sub>x</sub> is surrounded by carbon, which results in a  $^7\text{Li}$  chemical shift ( $-0.7$  ppm for sample Li = 0.04) that is closer to LiF’s reported value ( $-1.0$  ppm<sup>51</sup>).

$^7\text{Li}$  and  $^{19}\text{F}$   $T_1$  measurements were performed on the same series of samples in order to shed light on the particle size evolution of the LiF phase (Figure 15), and the trends observed for both nuclei are in agreement with each other. A significant increase in  $T_1$  upon discharge coincides with the sudden drop of potential in the electrochemical profile, the change being more noticeable between Li = 1.7 and 2.0. A significant reduction of  $T_1$  occurs at the beginning of charge and continues until approximately 3.92 V. These suggest that the LiF particle size increases significantly from Li = 1.0 until the end of discharge; this is followed by a drastic reduction on charging until the potential reaches around 3.8 V.

A more careful quantitative analysis of the  $^7\text{Li}$  (Figure S7a, SI) and  $^{19}\text{F}$  (Figure S7b, SI) MAS NMR spectra on the first discharge was performed to separate the contribution from the SEI components and the LiF. To compare the Li and F contents, we first analyze a sample in the region before the

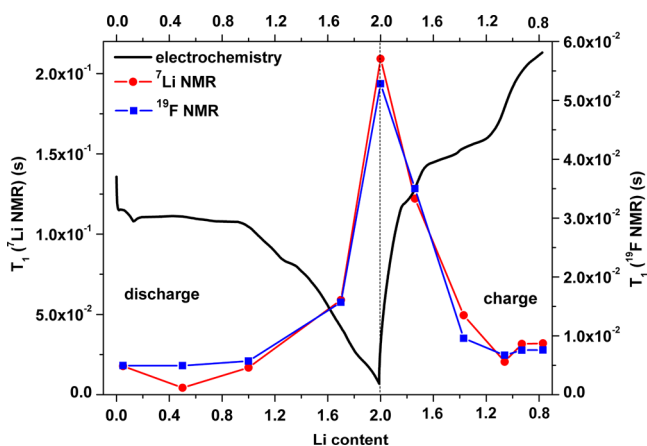


**Figure 15.**  ${}^7\text{Li}$  (red) and  ${}^{19}\text{F}$  (blue)  $T_1$  measurements for the samples shown in Figure 14. The electrochemical potential profile is shown for comparison.

onset of any significant side reactions (the  $\text{Li} = 1.0$  sample on discharge) and assume that the  ${}^7\text{Li}$  spectrum is dominated by  $\text{LiF}$ . The relative intensities of the resonances observed in the spectra from the other samples can then be scaled appropriately to extract the (diamagnetic)  $\text{Li}$  and  $\text{F}$  mole fractions. The results from this analysis are compared with phase fractions obtained from ex situ XANES and PDF measurements in Figure 10. The  $\text{CuF}_2$  phase fractions obtained from the LCA analysis of the ex situ XANES and the structure refinement of the ex situ PDFs are in excellent agreement, and the trend of  $\text{LiF}$  phase evolution evaluated from the  ${}^{19}\text{F}$  NMR mirrors the negative trend observed in the XANES and PDF data. This good match suggests that the formation of  $\text{LiF}$  is mainly the result of the  $\text{CuF}_2$  conversion. The nominal  $\text{LiF}$  content obtained by  ${}^7\text{Li}$  NMR is very different and tracks the overall  $\text{Li}$  content determined electrochemically. This observation confirms that electrolyte decomposition dominates at low potentials, producing SEI components (other than  $\text{LiF}$ ) that also contribute to the  ${}^7\text{Li}$  signal. A  ${}^{31}\text{P}$  MAS NMR spectrum of a sample extracted from a fully discharged battery at around 1 V (Figure 16) shows two resonances at 1 and  $-150$  ppm, which can be assigned to  $\text{Li}_3\text{PO}_4$  and  $\text{LiPF}_6$ , respectively.<sup>52</sup> The  $\text{PF}_6^-$  that is also observed in the early state of discharge ( $\text{Li} = 0.04$ ) (Figure S6, SI) is mostly due to  $\text{LiPF}_6$  residue from the electrolyte. The observation of  $\text{PO}_4^{3-}$  demonstrates that  $\text{Li}_3\text{PO}_4$

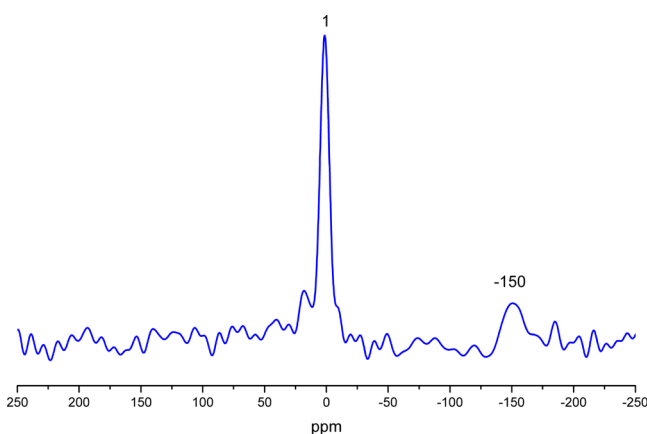


**Figure 16.**  ${}^{31}\text{P}$  MAS NMR spectrum of fully discharged  $\text{CCN-CuF}_2$  ( $\text{Li} = 2.0$ ).

is the main phosphate-containing product of electrolyte salt hydrolysis/degradation.

**3.6. Reaction Mechanisms. Discharge.** We now combine all of the results to discuss the various mechanisms that occur in this system. At the beginning of the discharge, a  $\text{CF}_x$  phase (identified by  ${}^{19}\text{F}$  MAS and  ${}^{19}\text{F}\rightarrow{}^{13}\text{C}$  CP-MAS NMR spectroscopy) reacts with  $\text{Li}^+$  prior to the onset of the  $\text{CuF}_2$  conversion, giving rise to the preplateau A at around 3.1 V (Figure 2). Upon further discharge, both in situ XANES and in situ PDF demonstrate a straightforward two-phase reaction mechanism for  $\text{CuF}_2$  conversion,  $\text{CuF}_2 + \text{Li} \rightarrow \text{Cu} + 2\text{LiF}$ . No evidence for a  $\text{Cu(I)}$  species, possibly formed via  $\text{Li}$  intercalation, is observed in the early state of discharge in either the first derivative of the difference XANES spectra (Figure 7c) or the CV study, where only one reduction peak B is present. Furthermore, no resonances corresponding to a  $\text{Li}_x\text{CuF}_2$  phase are seen in either the  ${}^7\text{Li}$  or  ${}^{19}\text{F}$  MAS NMR spectra. Therefore, a stable  $\text{Li}_x\text{CuF}_2$  intermediate phase, as proposed in the  $\text{CuF}_2$  thin film study,<sup>54</sup> is not formed in the  $\text{CCN-CuF}_2$  electrode on discharge.

As the  $\text{CuF}_2$  conversion proceeds, the operating potential starts to slope down at around  $\text{Li} = 1.0$  and small features  $\text{B}_\text{H}$ , C (Figure 2), and D (Figure 4) are observed [see the GITT results (Figure S1, SI)]. According to the Gibbs phase rule, a two-phase reaction under constant temperature and pressure should theoretically exhibit a flat potential plateau.<sup>55</sup> There is no evidence for a change in the mechanism of the conversion reaction [and a change from two-phase to single-phase (solid solution)] at  $\text{Li} = 1$ . Rather, the conversion reaction is associated with a larger overpotential at this point. This drop in potential enables additional side reactions ( $\text{B}_\text{H}$ , C, and eventually D) to occur, and since the kinetics of these reactions are faster, they increasingly predominate over the conversion reaction.

Feature  $\text{B}_\text{H}$  in the electrochemistry is always indistinct and sometimes not observed. Furthermore, it is only observed in the first discharge, suggestive of an irreversible process. The potential where this reaction occurs is higher than generally expected for electrolyte decomposition. We therefore ascribe it to the  $\text{Li}$  reaction with the hydrated  $\text{CuF}_2$  phases. As discussed in the CV section, features C and D (Figures 3 and 4) are attributed to the electrolyte decomposition on copper and carbon surfaces, respectively. The occurrence of electrolyte side reactions below 2 V is further verified by the comparison of total  $\text{Li}$  mole fraction ( $\text{LiF}$  and additional lithiated SEI components) obtained from ex situ  ${}^7\text{Li}$  NMR and the  $\text{LiF}$  mole fraction obtained by  ${}^{19}\text{F}$  NMR (Figure 10). Electrolyte decomposition results in  $\text{Li}$  salts (such as  $\text{LiF}$ ,  $\text{LiOCO}_2\text{R}$ ,  $\text{Li}_2\text{CO}_3$ ,<sup>26,33</sup> and  $\text{Li}_3\text{PO}_4$ ) that passivate the electrode surface, the presence of  $\text{Li}_3\text{PO}_4$  being confirmed by  ${}^{31}\text{P}$  NMR.  $\text{LiOCO}_2\text{R}$ ,  $\text{Li}_2\text{CO}_3$ ,<sup>26,33</sup> and  $\text{Li}_3\text{PO}_4$  give rise to  ${}^7\text{Li}$  resonances that are higher in frequency than the shift of  $\text{LiF}$  ( $-1$  ppm),<sup>51</sup> resulting in an overall shift of the  ${}^7\text{Li}$  resonance to higher frequencies beyond  $\text{Li} = 1$ . In the subsequent CV sweeps (Figure S2b, SI), less  $\text{Cu}$  is formed on reduction, and so less electrolyte decomposition on the  $\text{Cu}$  surface is expected. This is reflected by an intensity reduction/absence of peak C in association with the intensity reduction/absence of peak B; additionally, smaller currents are observed for peaks D and D', suggesting that the SEI layer on the carbon surface prevents further electrolyte decomposition.

In addition to the side reactions taking place after the kink in the electrochemical curve (at  $\text{Li} = 1.0$ ), a distinct change in the

rate at which the Cu and LiF particles grow in size is indicated by the structure refinements using the PDF data (Figure 9a) and NMR  $T_1$  measurements (Figure 15). Previous high-resolution transmission electron microscopy (HRTEM) studies on the pristine CCN-CuF<sub>2</sub> prepared using the same HBM technique reveal 8 nm CuF<sub>2</sub> nanoparticles present as large agglomerations (50–100 nm),<sup>7</sup> consistent with our measurements of an average particle size of 8.3 nm (PDF) and 10 nm (Scherrer analysis, XRD) for our system. The Scherrer equation gives a volume-weighted size, while the PDF measurement is weighted by the mole fraction, accounting for the difference in the two measured values.<sup>56</sup> Upon discharge, no significant change in the CuF<sub>2</sub> crystallite size extracted from the in situ PDF is observed. The size of the LiF phase, as reflected by the NMR  $T_1$  measurements, does not change noticeably at the beginning of discharge, while the size of the small Cu nanoparticles and the concentration of larger (>10 nm) particles increase according to the structure refinements of the corresponding PDFs.

We also observed a noticeable increase in overpotential at  $Li = 1.0$  in our previous studies of the CuF<sub>2</sub> system, with slightly larger CuF<sub>2</sub> particles (approximately 16 nm).<sup>5</sup> In that study, the rising overpotential was accompanied by a loss in crystallinity of the entire CuF<sub>2</sub> component, which we ascribed to particle cracking, possibly caused by Cu formation within these larger particles. A similar phenomenon is not seen here, possibly because the individual particles are slightly smaller. Furthermore, there is no reduction of CuF<sub>2</sub> particle size as the reaction proceeds, suggesting that particles largely react one by one, so that we do not see any clear evidence for any shrinking in the size of the CuF<sub>2</sub> nanoparticles. This is in agreement with recent in situ TEM studies of FeF<sub>2</sub> particles, where the particles were seen to react sequentially from the outside to the inside of both the original FeF<sub>2</sub> particle and the whole FeF<sub>2</sub>-C agglomerate.<sup>9</sup>

As discussed in our prior work,<sup>5</sup> the nucleation and growth of the different phases that form during the conversion reactions, and thus the morphologies and sizes of the particles within the nanocomposites, are governed by a number of factors, which include (i) the relative rates of diffusion of the cations, anions, and Cu atoms/ions through the original starting material, (any) intermediate phases, the final salts (LiF and SEI), and in the grain boundaries/interfaces between these phases and (ii) the electronic conductivities of the different components.<sup>3</sup> Li<sup>+</sup> ion diffusion in both CuF<sub>2</sub> and LiF is expected to be poor, but fluoride diffusion within the CuF<sub>2</sub> phase cannot be ruled out. CuF<sub>2</sub> is a poor electronic conductor, and hence, the Cu metal (and carbon) morphologies dictate the electronic wiring of the composite. No intermediate phases are present in this system, although the CuF<sub>2</sub>/Cu/LiF triple phase boundary, where Cu reduction occurs, will consist of poorly crystalline phases with poorly defined stoichiometries. The first CuF<sub>2</sub> particles to be reduced are those in direct or close contact to the carbon particles, due to the poor electronic conductivity of CuF<sub>2</sub>. Copper is extruded from the particles, and nanoparticles of LiF are formed. The LiF phase is in close contact to the Cu and CuF<sub>2</sub> surfaces, as suggested by <sup>7</sup>Li and <sup>19</sup>F MAS NMR, where a more negative chemical shift for the LiF signal is observed in the early state of discharge. Some fluoride ion migration may also occur through CuF<sub>2</sub> (as suggested previously), resulting in LiF coating of the entire reacting CuF<sub>2</sub> nanoparticle.<sup>5</sup> The formation of LiF should intrinsically lead to a higher overpotential due to its poor electronic conductivity. However, the formation of more Cu yields a larger interfacial area for the

conversion reaction to take place. The reaction continues, consuming particles buried more deeply in the agglomerate, promoted by the Cu wiring.

As the reaction approaches the kink position ( $Li = 1.0$ ), LiF increasingly covers the CuF<sub>2</sub> and Cu nanoparticles, leading to a larger overpotential due to LiF's poor electronic conductivity and low Li<sup>+</sup> diffusivity. Furthermore, the reaction front has moved deeper into the composite, increasing the electronic and ionic resistance associated with (i) the electronic wiring that connects the carbon (the source of electrons) and the reduction front and (ii) the ionic transport of the Li<sup>+</sup> ions from the electrolyte to the CuF<sub>2</sub> reaction front. The relative position of the kink (increasing overpotential) is probably related to the size of the CuF<sub>2</sub> agglomerate, the CuF<sub>2</sub> particle sizes, and the nature of the carbon-Cu wiring. Some sintering must occur as Cu particles larger than the size of the original CuF<sub>2</sub> particles are observed in the in situ PDF measurements. These are a minority component, particularly during the early stages of the conversion reaction, suggesting that the observation of large particles in prior ex situ XRD studies<sup>5</sup> may in part be a consequence of particle aging. However, the sintering increases as the reaction proceeds, which may lead to disconnected Cu particles (i.e., particles not wired to the carbon matrix), as also observed in the previous TEM study of fully discharged CuF<sub>2</sub>.<sup>7</sup> The presence of disconnected Cu particles may also increase the overpotential, since the CuF<sub>2</sub> particles in the core of the agglomerate are no longer wired to the carbon.

When the operating potential decreases until below 2.0 and 1.0 V, the electrolyte starts to decompose on the Cu and carbon surface successively, with each forming a passivating layer, leading to an even larger polarization. This results in even more difficult electronic and ionic transport and, consequently, a continuous increase in the overpotential. Furthermore, the conversion reaction results in a volume change of about 29% based on the crystalline densities, which will result in an expansion of the agglomerate. This expansion may result in cracks, exposing fresh surfaces for electrolyte decomposition and breaking Cu-Cu contacts, both increasing the overpotential. Eventually, when the electron transport pathways are all terminated by LiF and SEI products, the electrons and Li<sup>+</sup> ions can no longer reach the core of the initial CuF<sub>2</sub> agglomerate, leaving behind a small amount of unreacted CuF<sub>2</sub> in the center of the agglomerate. Further discharging to 0 V only induces more electrolyte reactions associated with carbon but does not reduce the amount of unreacted CuF<sub>2</sub>.

**Charge.** Upon charge, four different processes can be distinguished in the potential curve and CV (Figures 2 and 3), labeled as C', B<sub>1</sub>', B<sub>2</sub>', and D'. It has been reported that Cu metal dissolves in a wide range of organic solvents without passivation, mainly as Cu<sup>+</sup>.<sup>57,58</sup> Depending on the electrolyte, the dissolution voltage varies between 3.5 and 3.7 V vs Li<sup>+</sup>/Li.<sup>59</sup> For example, the thermodynamic equilibrium potential for the reaction  $Cu \rightarrow Cu^+ + e^-$  in an aqueous solution under standard conditions is 3.566 vs Li<sup>+</sup>/Li,<sup>26</sup> and a corrosion potential of 3.6 V was observed in a 1 M LiPF<sub>6</sub>/EC-DEC electrolyte.<sup>60</sup> Our battery, using Cu foil as cathode, shows a dissolution plateau at a similar voltage (3.5 V) (Figure S8, SI). Thus, we ascribe peak B<sub>1</sub>' at 3.58 V to Cu(0) to Cu(I) oxidation and B<sub>2</sub>' to the Cu(I) to Cu(II) or simultaneous Cu(0) to Cu(II) oxidation, in agreement with our in situ XANES analysis. Regarding the form of the dissolution products, a prior study revealed that the dissolution of Cu is not associated with any solid deposition

formation.<sup>59</sup> This is consistent with our PDF results, where no clear evidence for the presence of a third phase other than Cu and CuF<sub>2</sub> is observed either in situ or ex situ. The phase evolution from the PDF structure refinements and differential PDFs demonstrates only a small growth of the CuF<sub>2</sub> phase in the first two charge steps. The <sup>7</sup>Li and <sup>19</sup>F NMR and the T<sub>1</sub> results indicate a significant reduction in both quantity and the grain size of LiF upon charge before the rising-voltage region D' is reached. This suggests that a reaction consuming a large amount of LiF is taking place at B<sub>1</sub>' and B<sub>2</sub>'. Studies on copper dissolution have revealed that the presence of impurities such as H<sub>2</sub>O and HF, which facilitate the hydrolysis of LiPF<sub>6</sub> forming LiF, may considerably enhance the dissolution of Cu.<sup>26,61</sup> These prior studies correlate the reduction of LiF phase fraction with Cu dissolution, suggesting that the dissolution is associated with F<sup>-</sup> anions. As shown in the PCA analysis of the XANES spectra, upon oxidation of Cu to Cu<sup>+</sup>, a tetrahedrally coordinated Cu(I) complex ion such as [Cu<sup>I</sup>F<sub>4</sub>]<sup>3-</sup> (with a Cu environment similar to that found in CuCl) appears to be present. On further oxidation to Cu<sup>2+</sup>, a Cu(II) species, the majority of which has a Cu local environment similar to that found in CuF<sub>2</sub> is formed, possibly [Cu<sup>II</sup>F<sub>6</sub>]<sup>4-</sup>. On the basis of the combined capacity of regions B<sub>1</sub>' and B<sub>2</sub>', dissolution of approximately 30% of the Cu is expected, assuming that no other reactions occur at this voltage. If we then assume that the final dissolution product is [Cu<sup>II</sup>F<sub>6</sub>]<sup>4-</sup>, this copper dissolution consumes about 90% of the total amount of LiF, in order to form the complex ion [Cu<sup>II</sup>F<sub>6</sub>]<sup>4-</sup>. This rough calculation, however, is consistent with the almost complete loss of the LiF phase observed in the aforementioned <sup>7</sup>Li and <sup>19</sup>F MAS NMR, confirming that the Cu dissolution process consumes LiF. This therefore prevents CuF<sub>2</sub> reconversion from taking place, even at a potential as high as 4.5 V. It is worth noting that when the batteries were disassembled for ex situ experiments, a Cu<sup>2+</sup>-type greenish blue and/or a lusterless brown was sometimes noticed on the lithium metal, suggestive of the Cu<sup>2+</sup> ion migration and/or possibly Cu redeposition.<sup>26</sup> However, the formation of negatively charged copper(I) and -(II) ions most likely helps to reduce the extent of the redox shuttle mechanism involving Cu deposition.<sup>26</sup>

Interestingly, a decrease in the current associated with feature B<sub>1</sub>' in the CV plot (Figure 3) is associated with an increase in the current associated with feature C', C' being correlated with the reduction peak C in the anodic sweep. However, the current magnitude for feature B<sub>2</sub>' does not change significantly. Feature C is attributed to the electrolyte decomposition and formation of a passivating SEI layer on the Cu surface. The presence of such a passivating layer impedes the oxidation process B<sub>1</sub>', suggesting that the corresponding reaction from Cu(0) to Cu(I) is probably a kinetically controlled process. However, the formation of Cu(II) species is less affected. The assignment of reaction C' to the decomposition of the SEI formed during process C, is further supported by NMR results. The <sup>19</sup>F NMR on the sample collected at the charge state of 3.22 V (Figure 14b), which is just after the feature C' in the potential curve, shows about the same intensity as the one for the end of discharge Li = 2.0, suggesting that the majority of LiF does not participate in process C'. By contrast, the <sup>7</sup>Li NMR data for the same sample reveals a noticeable intensity reduction as compared to the end of discharge, indicating a decrease in the Li-containing components. These observations reflect a reduction in the amount of non-LiF components being associated with the degradation of the SEI formed on the Cu

surface. <sup>7</sup>Li and <sup>19</sup>F NMR confirm that LiF and Li<sub>2</sub>PO<sub>3</sub>F are formed during process D' due to electrolyte decomposition. The correlation between processes D' and D (SEI formation on carbon surface) suggests that the newly formed LiF is in close contact with carbon, rather than Cu metal. Therefore, only a small amount of this LiF phase will participate in the Cu dissolution or the Cu oxidation to form CuF<sub>2</sub>. The unreacted CuF<sub>2</sub> left after the first discharge can presumably react in the second cycle in part because the Cu and LiF dissolution removes some of the passivating LiF coating.

Many factors, such as ionic diffusion, electron transport, volume expansion, and SEI formation, are known to have a great impact on the reversibility of conversion reactions. In this specific case, however, the main reason for the poor reversibility is shown to be Cu dissolution and simultaneous LiF consumption. This should be contrasted with the highly reversible fluoride system FeF<sub>2</sub>. The potential for FeF<sub>2</sub> reconversion upon charge (~3.0 V) is far outside of the dissolution potential range (~4.0–4.6 V depending on the electrolyte composition and the type of salt) for Fe metal.<sup>2,7,59</sup> In contrast to Fe, the dissolution potential for Cu metal (~3.5–3.7 V) in an electrolyte composed of organic carbonates is about the same value as the theoretical potential for CuF<sub>2</sub> formation (3.55 V). Consequently, in the presence of the overpotentials that are typical for conversion reactions, Cu dissolution will take place and compete with the reconversion reaction Cu + 2LiF → CuF<sub>2</sub>, consuming the majority of the LiF phase formed upon discharge. Approaches should, therefore, be taken to prevent the dissolution from taking place, by for example (i) using appropriate surface coatings and/or additives to the electrolyte to enhance the stability of Cu metal at high potentials and (ii) replacing the organic solvent and salt with an electrolyte system that will not facilitate the Cu dissolution. The latter is challenging due to the often very similar solubilities of Li<sup>+</sup> and Cu<sup>+</sup>.

#### 4. CONCLUSION

An investigation of the conversion reaction mechanism for carbon-coated CuF<sub>2</sub> has been performed with an array of characterization tools providing a comprehensive understanding of the reactions that occur over multiple discharge/charge cycles. CV experiments and in situ XANES reveal multiple redox pairs, including a one-step lithiation step on discharge to form Cu directly and a two-step Cu oxidation on charge involving formation of an intermediate Cu(I) species most likely with a tetrahedral coordination. A correlation between SEI formation/decomposition and the Cu/carbon surface is demonstrated. The Cu(I) species formed on charge is eventually oxidized to an octahedrally coordinated Cu(II) complex anion. In situ PDF sheds light on the phase transformations and reveals that the majority of CuF<sub>2</sub> only participates in the first discharge, and very little or no CuF<sub>2</sub> formation takes place upon charge. NMR provides insight into the LiF phase, the SEI components, and also the impurity phases, i.e., CF<sub>x</sub>, which are all challenging to probe by aforementioned techniques. The size evolution of the LiF phase reflected by <sup>7</sup>Li and <sup>19</sup>F NMR T<sub>1</sub> measurements provides a link between the growth of LiF particles and the increase in overpotential.

The PDF measurements show that the amount of the small Cu nanoparticles grows at the beginning of the CuF<sub>2</sub> conversion, which enhances the electronic conductivity and helps compensate for the insulating effect from the LiF phase.

Since the size of the LiF phase is much bigger than that of Cu metal, the formed Cu is largely covered by an insulating LiF layer, helping to prevent sintering. Eventually this LiF coating serves to reduce Cu–Cu wiring, leading to a larger overpotential. In addition, SEI formation on the Cu surface enlarges the overpotential even more, and consequently, a continuous potential reduction is observed on discharge after about one Li has been inserted per  $\text{CuF}_2$  formula unit, even for our best performing electrodes.

The charging mechanism for  $\text{CuF}_2$  is fundamentally different from most other conversion materials, because the potential for Cu metal dissolution in an organic electrolyte is close to that of the reconversion reaction. Cu, therefore, dissolves in the electrolyte and consumes the LiF, thereby hindering the Cu to  $\text{CuF}_2$  transformation. In order to prevent the dissolution from taking place and to transform this material into a practical rechargeable battery system, approaches such as surface coating and/or electrolyte substitution are required to stabilize the Cu metal at high potentials.

## ■ ASSOCIATED CONTENT

### ■ Supporting Information

GITT for the first cycle; CVs in the potential window of 4.5–2.0 and 4.5–0.0 V; details of the PCA, TT, and LCA analyses on the XANES spectra for the first charge; PDF analyses on the first charge and second discharge; magnification of the  $^{19}\text{F}$  MAS NMR spectrum for the discharged sample at  $\text{Li} = 0.04$ ;  $^7\text{Li}$  and  $^{19}\text{F}$  MAS NMR spectra for the quantitative analysis; potential profile for the Cu dissolution. This material is available free of charge via the Internet at <http://pubs.acs.org>.

## ■ AUTHOR INFORMATION

### Corresponding Author

\*Phone: +44(0)1223336509. E-mail: [cpg27@cam.ac.uk](mailto:cpg27@cam.ac.uk).

### Notes

The authors declare no competing financial interest.

## ■ ACKNOWLEDGMENTS

We acknowledge the funding from the U.S. DOE BES via funding to the EFRC NECCES, an Energy Frontier Research Center funded by the U.S. Department of Energy, Office of Science, Office of Basic Energy Sciences under Award Number DE-SC0001294 (support for Rosa Robert and Lin-Shu Du) and EPSRC via the “nanoionics” programme grant (support for Xiao Hua). Use of the National Synchrotron Light Source (NSLS), Brookhaven National Laboratory (BNL), was supported by the U.S. Department of Energy, Office of Science, Office of Basic Energy Sciences, under Contract No. DE-AC02-98CH10886. Use of the Advanced Photon Source, an Office of Science User Facility operated for the U.S. Department of Energy (DOE) Office of Science by Argonne National Laboratory, was supported by the U.S. DOE under Contract No. DE-AC02-06CH11357. We thank Dr. Dongli Zeng, Dr. Sylvia Britto, Dr. Yan-Yan Hu, Hao Liu, Rowan K. Leary, Dr. Olaf J. Borkiewicz, and Dr. Baris Key for their kind help with this project. We are also grateful to Profs. Jean-Marie Tarascon, Glenn G. Amatucci, and Shirley Meng for insightful discussions.

## ■ REFERENCES

- (1) Tarascon, J.; Grugeon, S.; Morcrette, M.; Laruelle, S.; Rozier, P.; Poizot, P. New Concepts for the Search of Better Electrode Materials for Rechargeable Lithium Batteries. *C. R. Chim.* **2005**, *8*, 9–15.
- (2) Amatucci, G. G.; Pereira, N. Fluoride Based Electrode Materials for Advanced Energy Storage Devices. *J. Fluorine Chem.* **2007**, *128*, 243–262.
- (3) Li, H.; Balaya, P.; Maier, J. Li-Storage Via Heterogeneous Reaction in Selected Binary Metal Fluorides and Oxides. *J. Electrochem. Soc.* **2004**, *151*, A1878–A1885.
- (4) Badway, F.; Mansour, A. N.; Pereira, N.; Al-Sharab, J. F.; Cosandey, F.; Plitz, I.; Amatucci, G. G. Structure and Electrochemistry of Copper Fluoride Nanocomposites Utilizing Mixed Conducting Matrices. *Chem. Mater.* **2007**, *19*, 4129–4141.
- (5) Yamakawa, N.; Jiang, M.; Grey, C. P. Investigation of the Conversion Reaction Mechanisms for Binary Copper(II) Compounds by Solid-State NMR Spectroscopy and X-ray Diffraction. *Chem. Mater.* **2009**, *21*, 3162–3176.
- (6) Lee, D. H.; Carroll, K. J.; Calvin, S.; Jin, S.; Meng, Y. S. Conversion Mechanism of Nickel Fluoride and NiO-Doped Nickel Fluoride in Li Ion Batteries. *Electrochim. Acta* **2012**, *59*, 213–221.
- (7) Wang, F.; Robert, R.; Chernova, N. A.; Pereira, N.; Omenya, F.; Badway, F.; Hua, X.; Ruotolo, M.; Zhang, R.; Wu, L.; et al. Conversion Reaction Mechanisms in Lithium Ion Batteries: Study of the Binary Metal Fluoride Electrodes. *J. Am. Chem. Soc.* **2011**, *133*, 18828–18836.
- (8) Bervas, M.; Mansour, A. N.; Yoon, W. S.; Al-Sharab, J. F.; Badway, F.; Cosandey, F.; Klein, L. C.; Amatucci, G. G. Investigation of the Lithiation and Delithiation Conversion Mechanisms of Bismuth Fluoride Nanocomposites. *J. Electrochem. Soc.* **2006**, *153*, A799–A808.
- (9) Wang, F.; Yu, H.-C.; Chen, M.-H.; Wu, L.; Pereira, N.; Thornton, K.; Van der Ven, A.; Zhu, Y.; Amatucci, G. G.; Graetz, J. Tracking Lithium Transport and Electrochemical Reactions in Nanoparticles. *Nat. Commun.* **2012**, *3*, 1201.
- (10) Patterson, A. L. The Scherrer Formula for X-ray Particle Size Determination. *Phys. Rev.* **1939**, *56*, 978–982.
- (11) Scardi, P.; Leoni, M.; Delhez, R. Line Broadening Analysis Using Integral Breadth Methods: A Critical Review. *J. Appl. Crystallogr.* **2004**, *37*, 381–390.
- (12) Balzar, D. Profile Fitting of X-ray Diffraction Lines and Fourier Analysis of Broadening. *J. Appl. Crystallogr.* **1992**, *25*, 559–570.
- (13) Mukerjee, S.; Thurston, T. R.; Jisrawi, N. M.; Yang, X. Q.; McBreen, J.; Daroux, M. L.; Xing, X. K. Structural Evolution of  $\text{Li}_x\text{Mn}_2\text{O}_4$  in Lithium-Ion Battery Cells Measured In Situ Using Synchrotron X-Ray Diffraction Techniques. *J. Electrochem. Soc.* **1998**, *145*, 466–472.
- (14) Ravel, B.; Newville, M. Athena, Artemis, Hephaestus: Data Analysis for X-Ray Absorption Spectroscopy Using IFEFFIT. *J. Synchrotron Radiat.* **2005**, *12*, 537–541.
- (15) Borkiewicz, O. J.; Shyam, B.; Wiaderek, K. M.; Kurtz, C.; Chupas, P. J.; Chapman, K. W. The Ampix Electrochemical Cell: A Versatile Apparatus for In Situ X-ray Scattering and Spectroscopic Measurements. *J. Appl. Crystallogr.* **2012**, *45*, 1261–1269.
- (16) Wiaderek, K. M.; Borkiewicz, O. J.; Castillo-Martínez, E.; Robert, R.; Pereira, N.; Amatucci, G. G.; Grey, C. P.; Chupas, P. J.; Chapman, K. W. Comprehensive Insights into the Structural and Chemical Changes in Mixed-Anion FeOF Electrodes by Using Operando PDF and NMR Spectroscopy. *J. Am. Chem. Soc.* **2013**, *135*, 4070–4078.
- (17) Takeshi, E.; Simon, J. L. B. *Underneath the Bragg Peaks Structural Analysis of Complex Materials*; Pergamon: New York, 2012.
- (18) Hammersley, A. P.; Svensson, S. O.; Hanfland, M.; Fitch, A. N.; Hausermann, D. Two-Dimensional Detector Software: From Real Detector to Idealised Image or Two-Theta Scan. *High Pressure Res.* **1996**, *14*, 235–248.
- (19) Qiu, X.; Thompson, J. W.; Billinge, S. J. L. PDFgetX2: A GUI-Driven Program to Obtain the Pair Distribution Function from X-Ray Powder Diffraction Data. *J. Appl. Crystallogr.* **2004**, *37*, 678.

- (20) Chupas, P. J.; Qiu, X.; Hanson, J. C.; Lee, P. L.; Grey, C. P.; Billinge, S. J. L. Rapid-Acquisition Pair Distribution Function (RAPDF) Analysis. *J. Appl. Crystallogr.* **2003**, *36*, 1342–1347.
- (21) Chapman, K. W.; Chupas, P. J.; Halder, G. J.; Hriljac, J. A.; Kurtz, C.; Greve, B. K.; Ruschman, C. J.; Wilkinson, A. P. Optimizing High-Pressure Pair Distribution Function Measurements in Diamond Anvil Cells. *J. Appl. Crystallogr.* **2010**, *43*, 297–307.
- (22) Farrow, C. L.; Juhas, P.; Liu, J. W.; Bryndin, D.; Božin, E. S.; Bloch, J.; Proffen, T.; Billinge, S. J. L. Pdffit2 and Pdgui: Computer Programs for Studying Nanostructure in Crystals. *J. Phys.: Condens. Matter* **2007**, *19*, 335219.
- (23) Choi, Y.-K.; Chung, K.-i.; Kim, W.-S.; Sung, Y.-E.; Park, S.-M. Suppressive Effect of  $\text{Li}_2\text{CO}_3$  on Initial Irreversibility at Carbon Anode in Li-Ion Batteries. *J. Power Sources* **2002**, *104*, 132–139.
- (24) Demeaux, J.; Cailion-Caravanier, M.; Galiano, H.; Lemordant, D.; Claude-Montigny, B.  $\text{LiNi}_{0.4}\text{Mn}_{1.6}\text{O}_4$ /Electrolyte and Carbon Black/Electrolyte High Voltage Interfaces: To Evidence the Chemical and Electronic Contributions of the Solvent on the Cathode–Electrolyte Interface Formation. *J. Electrochem. Soc.* **2012**, *159*, A1880–A1890.
- (25) Aurbach, D.; Levi, M. D.; Levi, E.; Schechter, A. Failure and Stabilization Mechanisms of Graphite Electrodes. *J. Phys. Chem. B* **1997**, *101*, 2195–2206.
- (26) Arora, P. Capacity Fade Mechanisms and Side Reactions in Lithium-Ion Batteries. *J. Electrochem. Soc.* **1998**, *145*, 3647–3667.
- (27) Xu, K. Nonaqueous Liquid Electrolytes for Lithium-Based Rechargeable Batteries. *Chem. Rev.* **2004**, *104*, 4303–4418.
- (28) Gmitter, A. J.; Badway, F.; Rangan, S.; Bartynski, R. A.; Halajko, A.; Pereira, N.; Amatucci, G. G. Formation, Dynamics, and Implication of Solid Electrolyte Interphase in High Voltage Reversible Conversion Fluoride Nanocomposites. *J. Mater. Chem.* **2010**, *20*, 4149–4161.
- (29) Dahn, J. Phase Diagram of  $\text{Li}_x\text{C}_6$ . *Phys. Rev. B* **1991**, *44*, 9170–9177.
- (30) Wang, H.; Yoshio, M. Carbon-Coated Natural Graphite Prepared by Thermal Vapor Decomposition Process, a Candidate Anode Material for Lithium-Ion Battery. *J. Power Sources* **2001**, *93*, 123–129.
- (31) Dahn, J. R.; Zheng, T.; Liu, Y.; Xue, J. S. Mechanisms for Lithium Insertion in Carbonaceous Materials. *Science* **1995**, *270*, 590–593.
- (32) Wu, G. T.; Wang, C. S.; Zhang, X. B.; Yang, H. S.; Qi, Z. F.; He, P. M.; Li, W. Z. Structure and Lithium Insertion Properties of Carbon Nanotubes. *J. Electrochem. Soc.* **1999**, *146*, 1696–1701.
- (33) Verma, P.; Maire, P.; Novák, P. A Review of the Features and Analyses of the Solid Electrolyte Interphase in Li-Ion Batteries. *Electrochim. Acta* **2010**, *55*, 6332–6341.
- (34) Kau, L. S.; Spira-Solomon, D. J.; Penner-Hahn, J. E.; Hodgson, K. O.; Solomon, E. I. X-ray Absorption Edge Determination of the Oxidation State and Coordination Number of Copper. Application to the Type 3 Site in *Rhus vernicifera* Laccase and Its Reaction with Oxygen. *J. Am. Chem. Soc.* **1987**, *109*, 6433–6442.
- (35) Yamamoto, T. Assignment of Pre-Edge Peaks in K-Edge X-Ray Absorption Spectra of 3d Transition Metal Compounds: Electric Dipole or Quadrupole? *X-Ray Spectrom.* **2008**, *37*, 572–584.
- (36) Choy, J.-H.; Yoon, J.-B.; Jung, H. Polarization-Dependent X-Ray Absorption Spectroscopic Study of  $[\text{Cu}(\text{cyclam})]^{2+}$ -Intercalated Saponite. *J. Phys. Chem. B* **2002**, *106*, 11120–11126.
- (37) Mansour, A. N.; Badway, F.; Yoon, W. S.; Chung, K. Y.; Amatucci, G. G. In Situ X-ray Absorption Spectroscopic Investigation of the Electrochemical Conversion Reactions of  $\text{CuF}_2\text{–MoO}_3$  Nanocomposite. *J. Solid State Chem.* **2010**, *183*, 3029–3038.
- (38) Ebert, F.; Woitinek, H. Kristallstrukturen Von Fluoriden. II.  $\text{HgF}_2$ ,  $\text{HgF}_3$ ,  $\text{CuF}$  und  $\text{CuF}_2$ . *Z. Anorg. Allg. Chem.* **1933**, *210*, 269–272.
- (39) Mccauley, D. A. (Standard Oil Co., USA). Preparation of Cuprous Fluoride. U.S. Patent 2817576, 1957.
- (40) Walsh, A.; Catlow, C. R. A.; Galvelis, R.; Scanlon, D. O.; Schiffmann, F.; Sokol, A. A.; Woodley, S. M. Prediction on the Existence and Chemical Stability of Cuprous Fluoride. *Chem. Sci.* **2012**, *3*, 2565–2569.
- (41) Myung, S.-T.; Sasaki, Y.; Sakurada, S.; Sun, Y.-K.; Yashiro, H. Electrochemical Behavior of Current Collectors for Lithium Batteries in Non-Aqueous Alkyl Carbonate Solution and Surface Analysis by ToF-SIMS. *Electrochim. Acta* **2009**, *55*, 288–297.
- (42) Wang, Q.; Hanson, J. C.; Frenkel, A. I. Solving the Structure of Reaction Intermediates by Time-Resolved Synchrotron X-Ray Absorption Spectroscopy. *J. Chem. Phys.* **2008**, *129*, 234502.
- (43) Gaur, A.; Shrivastava, B. A Comparative Study of the Methods of Speciation Using X-ray Absorption Fine Structure. *Acta Phys. Polym., A* **2012**, *121*, 647–652.
- (44) Karg, M.; Scholz, G.; König, R.; Kemnitz, E. Mechanistic Insight into Formation and Changes of Nanoparticles in  $\text{MgF}_2$  Sols Evidenced by Liquid and Solid State NMR. *Dalton Trans.* **2012**, *41*, 2360–2366.
- (45) Youngman, R. E.; Sen, S. A High-Resolution  $^{19}\text{F}$  NMR Spectroscopic Study of Barium Fluorozirconate Glasses and Related Crystals. *Solid State Nucl. Magn. Reson.* **2005**, *27*, 77–89.
- (46) Dou, X.; Mohan, D.; Pittman, C. U., Jr.; Yang, S. Remediating Fluoride from Water Using Hydrous Zirconium Oxide. *Chem. Eng. J.* **2012**, *198–199*, 236–245.
- (47) R. Krawietz, T.; F. Haw, J. Characterization of Poly(carbon monofluoride) by  $^{19}\text{F}$  and  $^{19}\text{F}$  to  $^{13}\text{C}$  Cross Polarization MAS NMR Spectroscopy. *Chem. Commun.* **1998**, 2151–2152.
- (48) Leifer, N. D.; Johnson, V. S.; Ben-Ari, R.; Gan, H.; Lehnes, J. M.; Guo, R.; Lu, W.; Muffoletto, B. C.; Reddy, T.; Stallworth, P. E.; et al. Solid-State NMR Studies of Chemically Lithiated  $\text{CF}_x$ . *J. Electrochem. Soc.* **2010**, *157*, A148–A154.
- (49) Zhang, W.; Dubois, M.; Guerin, K.; Bonnet, P.; Kharbache, H.; Masin, F.; Kharitonov, A. P.; Hamwi, A. Effect of Curvature on C–F Bonding in Fluorinated Carbons: From Fullerene and Derivatives to Graphite. *Phys. Chem. Chem. Phys.* **2010**, *12*, 1388–1398.
- (50) Levi, M. D.; Aurbach, D. The Application of Electroanalytical Methods to the Analysis of Phase Transitions During Intercalation of Ions into Electrodes. *J. Solid State Electrochem.* **2007**, *11*, 1031–1042.
- (51) Meyer, B. M.; Leifer, N.; Sakamoto, S.; Greenbaum, S. G.; Grey, C. P. High Field Multinuclear NMR Investigation of the SEI Layer in Lithium Rechargeable Batteries. *Electrochem. Solid-State Lett.* **2005**, *8*, A145–A148.
- (52) Plakhotnyk, A. V.; Ernst, L.; Schmutzler, R. Hydrolysis in the System  $\text{LiPF}_6\text{–Propylene Carbonate–Dimethyl Carbonate–H}_2\text{O}$ . *J. Fluorine Chem.* **2005**, *126*, 27–31.
- (53) Guérin, K.; Yazami, R.; Hamwi, A. Hybrid-Type Graphite Fluoride as Cathode Material in Primary Lithium Batteries. *Electrochem. Solid-State Lett.* **2004**, *7*, A159–A162.
- (54) Cui, Y.-H.; Xue, M.-Z.; Zhou, Y.-N.; Peng, S.-M.; Wang, X.-L.; Fu, Z.-W. The Investigation on Electrochemical Reaction Mechanism of  $\text{CuF}_2$  Thin Film with Lithium. *Electrochim. Acta* **2011**, *56*, 2328–2335.
- (55) Huggins, R. A. *Advanced Batteries: Materials Science Aspects*; Springer: New York, 2008.
- (56) Popa, N. C.; Balzar, D. An Analytical Approximation for a Size-Broadened Profile Given by the Lognormal and Gamma Distributions. *J. Appl. Crystallogr.* **2002**, *35*, 338–346.
- (57) Mann, C. K.; Barnes, K. K. *Electrochemical Reactions in Nonaqueous Systems*; Dekker: New York, 1970.
- (58) Kawakita, J.; Kobayashi, K. Anodic Polarization Behavior of Copper in Propylene Carbonate. *J. Power Sources* **2001**, *101*, 47–52.
- (59) Whitehead, A. H.; Schreiber, M. Current Collectors for Positive Electrodes of Lithium-Based Batteries. *J. Electrochem. Soc.* **2005**, *152*, A2105–A2113.
- (60) Iwakura, C.; Fukumoto, Y.; Inoue, H.; Ohashi, S.; Kobayashi, S.; Tada, H.; Abe, M. Electrochemical Characterization of Various Metal Foils as a Current Collector of Positive Electrode for Rechargeable Lithium Batteries. *J. Power Sources* **1997**, *68*, 301–303.
- (61) Zhao, M.; Dewald, H. D.; Staniewicz, R. J. Quantitation of the Dissolution of Battery-Grade Copper Foils in Lithium-Ion Battery Electrolytes by Flame Atomic Absorption Spectroscopy. *Electrochim. Acta* **2004**, *49*, 683–689.